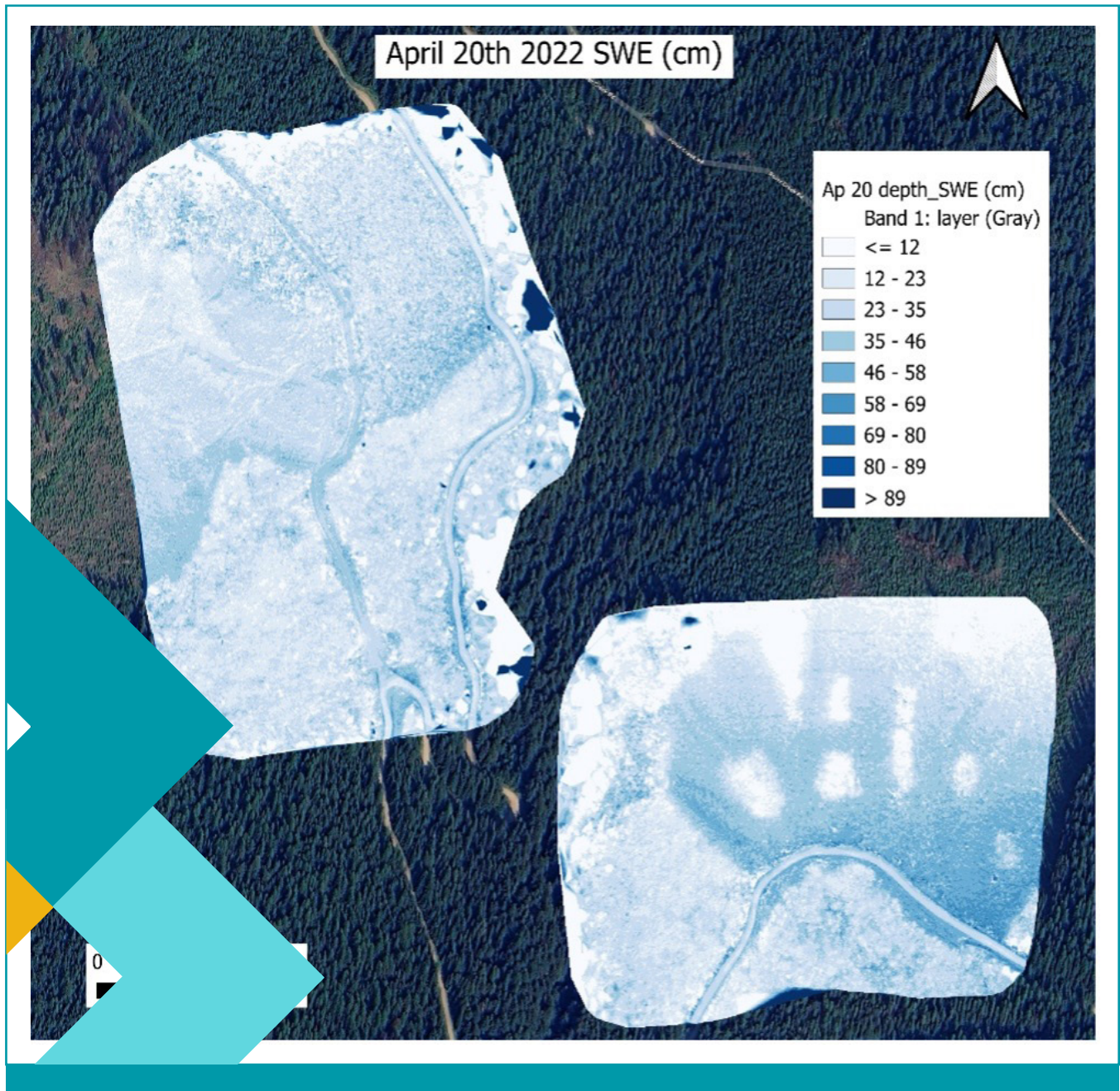


# Utilizing UAV LiDAR-derived Snow Surfaces for Assessing Forest & Aspect Effects on Snow Depth & SWE



This study has been undertaken by a team of qualified researchers. Selkirk Innovates research should not be considered a complete analysis. We make no warranty as to the quality, accuracy, or completeness of the data. Selkirk College will not be liable for any direct or indirect loss resulting from the use of or reliance on these study outcomes.

Selkirk Innovates acknowledges the following funding support for this project.

- Natural Sciences and Engineering Research Council of Canada College and Community Innovation Program
- Mitacs through the Mitacs Accelerate Program.
- The Government of Canada through Natural Resources Canada's Green Jobs - Science and Technology Internship Program, as part of the Youth Employment and Skills Strategy. Par le gouvernement du Canada par l'entremise du Programme de stages en sciences et technologie - Emplois verts de Ressources naturelles Canada dans le cadre de la Stratégie emploi et compétences jeunesse.

Project team: Selkirk Innovates: Kim Green, PhD., P.Geo., Kristina Deenik, MSc, BIT, Taylor Clark, MSc., Apex Geoscience Consultants Ltd: Cydne Potter, MSc., GIT.

**Recommended Citation:** Selkirk Innovates (2025). Utilizing UAV LiDAR-derived Snow Surfaces for Assessing Forest and Aspect Effects on Snow Depth and SWE. Selkirk College. <https://sc.arcabc.ca/>



Natural Sciences and Engineering  
Research Council of Canada

Conseil de recherches en sciences  
naturelles et en génie du Canada

Canada



*On behalf of Selkirk College, I (we) acknowledge that we operate and serve learners on the unceded traditional territories of the Sinixt (Lakes), the Syilx (Okanagan), the Ktunaxa, and the Secwepemc (Shuswap) peoples.*

## Executive Summary

This report presents the results of a UAV LiDAR-based study conducted in the Rover Creek watershed in the Kootenay region of British Columbia during the 2022 snowmelt season. The research explored how forest stand maturity and slope aspect affect snow accumulation and melt dynamics, with a focus on quantifying hydrological recovery following forest disturbance. UAV-mounted LiDAR was used to generate high-resolution snow depth models across two hillslope sites with contrasting aspects—north-facing Site A and east-facing Site B. These models were converted to snow water equivalent (SWE) using regression equations derived from prior field data, enabling spatially continuous analysis of peak SWE and ablation rates.

The study found that forest maturity significantly influences snow processes. Open stands consistently showed higher peak SWE and faster ablation rates than juvenile and mature stands. In open areas, slope aspect played a dominant role, with north-facing slopes accumulating more snow and melting more slowly than east- and southeast-facing slopes. In contrast, mature stands exhibited minimal differences in SWE and ablation across aspects, indicating that canopy cover moderates the energy balance at the snow surface.

Hydrological recovery patterns varied between sites. Site A showed slower recovery, particularly in ablation rates, while Site B exhibited more rapid recovery, although variability was observed between adjacent juvenile stands. These differences were attributed to aspect-driven variations in energy input, with north-facing juvenile stands displaying delayed recovery compared to east-facing ones. The variable retention mature stand in Site B behaved more like an open stand in terms of ablation, suggesting that a reduction in canopy cover influences snowmelt energy availability even when mature trees are present.

The study highlights the utility of UAV LiDAR in characterizing snow-forest interactions and provides insights for improving hydrological models and forest management strategies in snow-dominated mountain watersheds. It also emphasizes the need for site-specific snow depth to SWE calibration when applying hydrological recovery models, given the complex interplay of forest structure, aspect, and local topography.

# Contents

Executive Summary.....	i
1.0 Introduction .....	1
1.1 Research Team .....	2
1.2 Study Area .....	3
2.0 Methods.....	7
2.1 Field Data Collection .....	7
2.2 Data Processing.....	7
3.0 Results.....	15
3.1 LiDAR-derived forest stand metrics .....	15
3.2 Trends in peak SWE and ablation rates from LiDAR-derived snow depth.....	15
3.4 Hydrological Recovery of Peak SWE and Ablation with Tree Height .....	24
4.0 Discussion.....	26
Forest Maturity and Peak SWE .....	26
Forest maturity and Ablation.....	27
Aspect Effects on peak SWE and Ablation .....	27
Hydrological Recovery Patterns.....	27
Unexpected Results and Outliers.....	28
Implications and Future Directions.....	28
Key findings include: .....	29
6.0 Citations .....	29
Appendix 1. Equipment used in field data collection .....	32
Appendix 2 - Snow Water Equivalent from Snow Depth – Investigation of snow density derivation approaches.....	33
Appendix 3. Statistical test results.....	35

## 1.0 Introduction

Changes to forest structure due to logging, forest fires, or beetle kill can have long-lasting effects on the hydrological response of a watershed leading to changes in the timing of spring snowmelt, increases in the frequency and magnitude of flooding, increases in the duration of low flows and decreases in water quality. In snowy regions, trees can reduce the amount of snow that accumulates on the ground through the processes of interception and evapotranspiration and can delay and reduce the rate of snowmelt by shading the snowpack from incoming solar radiation (Hedstrom and Pomeroy, 1998; Varhola et al., 2010). The capacity of the forest to influence snow processes depends in part on the characteristics of the forest stand including tree height and stem density (Winkler et al., 2005; Ellis et al., 2011; Varhola et al., 2010). Taller trees with longer crown heights and stands with higher stem densities have been shown to intercept more snow compared to smaller trees and more open stands with lower stem densities (Winkler et al., 2005; Potter et al., 2024). Other studies in forested snowmelt watersheds have shown that slope aspects play a role in the extent to which forests affect snow accumulation and snowmelt with less pronounced effects between forest and openings on north aspect slopes compared to south aspect slopes (Jost et al., 2007; Ellis et al., 2011).

Hydrological recovery refers to when a regenerating forest stand returns to the pre-harvest condition, in terms of its ability to intercept precipitation and shade the snowpack. Previous studies have quantified hydrological recovery of a forest stand by developing relationships between stand attributes of height and canopy density (or crown closure) and peak snow water equivalent (peak SWE) and ablation rates averaged for the below stand area (Hudson, 2000; Winkler and Boon, 2015; Potter et al., 2024). Considerable uncertainty remains in published hydrological recovery relationships, particularly regarding their transferability beyond the original study sites and broader applicability across diverse ecological and climatic contexts. Except for Potter and others (2024), these past studies relied on manual snow sampling methods with low sampling density, which calculated a single value of SWE as the average of a limited number of equally spaced snow core samples collected along a single elevation contour or across a grid. A recent investigation of snow depth variability in forest stands using terrestrial handheld mobile LiDAR (Potter, 2024) has revealed complex spatial patterns of snow accumulation in juvenile and clearcut stands reducing the confidence in recovery curves based on averaging of limited sampling densities. Furthermore, most of the foundational studies underpinning Equivalent Clearcut Area (ECA) calculations in British Columbia have not incorporated aspect (the direction the slope is facing), despite its potential influence on snow accumulation and melt dynamics. The lack of information regarding hydrological recovery rates for regenerating forest stands in mountainous regions, where slope aspect is always a consideration, has resulted in additional uncertainty when applying published hydrological recovery relationships derived in flat terrain.

Light Detection and Ranging (LiDAR) technology which uses pulses of light to provide a 3D model of a surface, has proven to be a fast and effective way to capture the topography of snow surfaces and create Digital Terrain Models (DTM) and is ideally suited for application in the study of hydrological recovery of forest stands (Deems et al., 2006; 2013, Potter et al., 2024). In this application, the surface elevation points in a snow-free scan are subtracted from the surface elevation points in a snow-filled scan to determine



snow depth which is subsequently converted to snow water equivalent (SWE in cm) using established snow depth to snow density relationships (BC MoE, 1981). DTMs created from LiDAR point clouds vary in precision depending on the type of scanner used and method of collection. Data collection using handheld ground-based LiDAR scanning methods results in high density point clouds and very high resolution DTMs; however, complex terrain can limit accessibility. LiDAR collected using an unmanned aerial vehicle (UAV) can overcome terrain accessibility issues but may not adequately penetrate the forest canopy to define a sufficiently detailed snow surface elevation model. Technological advancements are rapidly improving LiDAR canopy penetration and the density of ground returns even in dense forests. A preliminary study investigating differences between average snow depth measurements obtained from DTMs that were produced from a UAV-mounted LiDAR (L1 - DJI) scanner and a handheld (GeoSLAM) scanner was undertaken to determine the suitability of the UAV LiDAR data collection method (Deenik et al., 2022). It was found that the UAV LiDAR scans could adequately capture the beneath-canopy snow surface, particularly in more open areas where high density ground returns were obtained beneath the canopy.

Once it was determined that UAV LiDAR could be used to reliably generate below-canopy snow surface rasters, the Selkirk Innovates team investigated the influence of forest stand maturity and slope aspect on peak SWE and ablation rates during the 2022 snowmelt season. The UAV LiDAR allowed for a larger study area to be scanned compared to earlier hand-held GeoSLAM based surveys, allowing us to investigate forest effects on snow processes for a wider range of forest stands and slope aspects. The 2022 field program at the Rover Creek study area (near Castlegar, BC) included repeated UAV LiDAR flights from peak snow to snow free conditions with the goal of improving the understanding of hydrological recovery of forest stands in Kootenay mountain watersheds. This study introduces a novel approach by using drone-based LiDAR to characterize the influence of forest removal and regrowth across aspects on peak SWE and ablation rates, advancing previous research that relied on ground-based LiDAR data from GeoSLAM scanners in limited areas (Potter et al., 2024).

## 1.1 Research Team

The research team for this project is shown in Table 1 and included Selkirk Innovates research assistants, an advanced UAV pilot, and several student interns. Fieldwork was conducted with at least two team members on-site, and 15 visits were made throughout the snowmelt season to ensure comprehensive data collection. Data processing and analysis were carried out by student interns with the guidance of research assistants.

*Table 1. Selkirk Innovates individuals involved during the 2022 project and their responsibilities.*

Name & Credentials		Responsibility
Kim Green, PhD, PGeo		Project lead and reporting
Cydne Potter, MSc, GIT		Data analysis and reporting
David Greaves, MGISA	Site prep, UAV pilot, LiDAR data management and processing	
Kristina Deenik, MSc, BIT		Field data collection, data analysis and reporting
Taylor Clark, MRM		Data analysis and reporting
Various student interns		Field data collection

## 1.2 Study Area

The study area was located within the Rover Creek watershed in the Bonnington range between Nelson and Castlegar, British Columbia (Figure 1). For this study, two adjacent sites located at approximately 1,500-m elevation were chosen for hillslope-scale comparisons between primarily north (Site A, 1408m-1550m) and east (Site B, 1368m-1519m) aspects (Figure 2). Within the two sites, individual stands were selected to represent a range of forest maturity including recently replanted open (O), juvenile (J), mature (M), and one pest-disturbed mature stand that is characterized as a variable retention stand (variable).

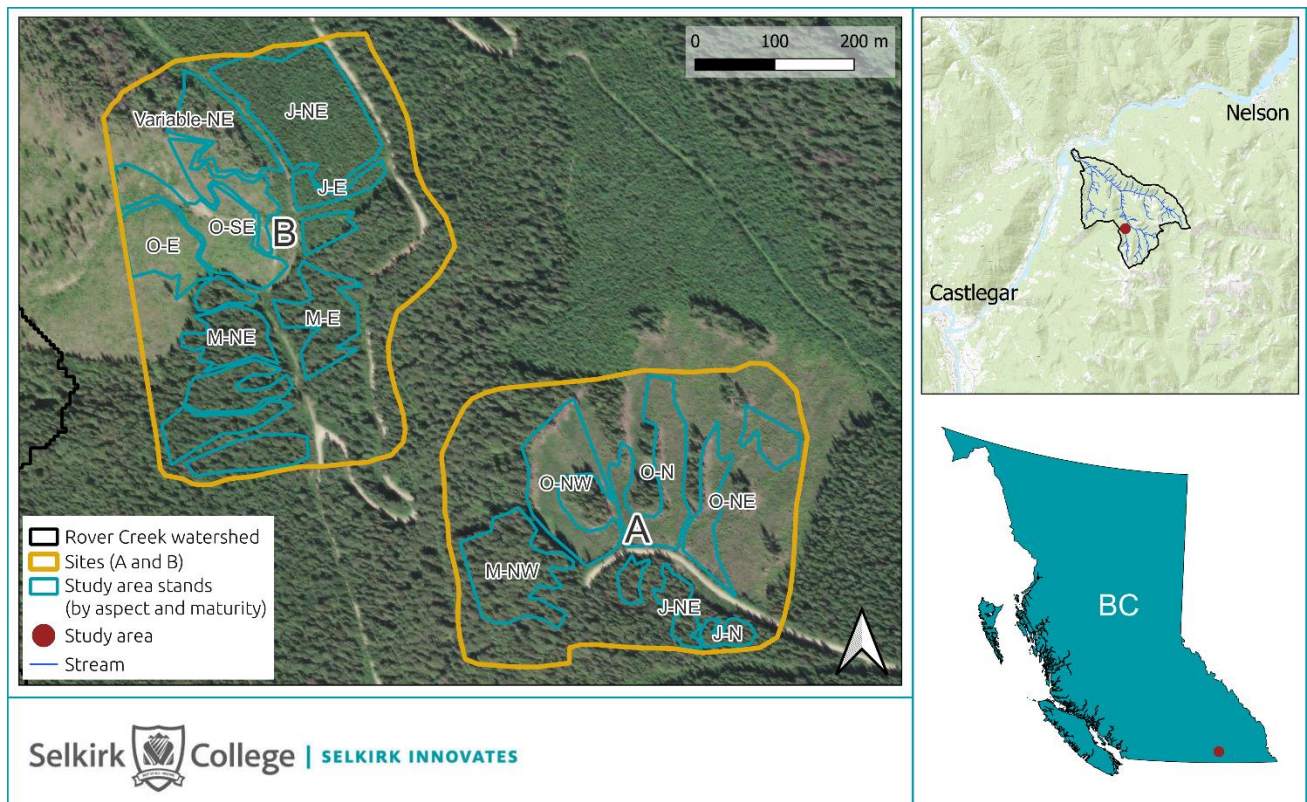


Figure 1. Rover Creek Study area Sites A and B outlined in yellow. The location of stands within each Site organized according to slope aspect (NE, E, NW, N, and SE) and stand maturity including open (O), juvenile (J), and mature (M) are outlined in teal.

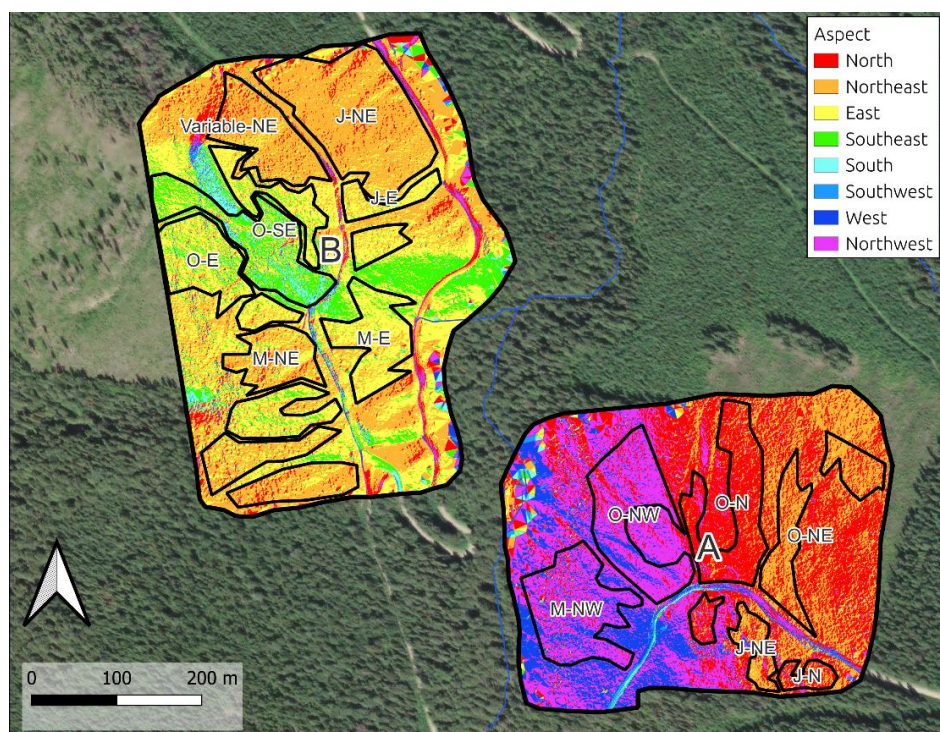


Figure 2. Aspect distributions across stands in Sites A and B.

Topographic information including stand area, elevation, slope aspect, and slope percent were derived from a 1-meter resolution 2014 LiDAR DTM provided by Kalesnikoff Lumber Company Ltd. Tree species distributions and stand ages were determined from information recorded in the province of British Columbia's Vegetation Resource Inventory database (downloaded from <https://catalogue.data.gov.bc.ca/group/vegetation-resource-inventory>). Information on the area, elevation range, median aspect, median slope, stand age and dominate tree species for each stand is presented in Table 2.

**Table 2** Topographic characteristics, stand age, and tree species composition for open (O), juvenile (J), mature (M), and variable height (variable) stands in sites A and B. Stand age denoted by an \* indicates stands where a 1968 airphoto was used to estimate age. Tree species codes shown here are defined in Table 3.

Stand	AOI area (ha)	Elevation (m) (min, mean, max)	Aspect median (°)	Slope mean (°)	Stand age (years)	Tree species (%)
A_J-N	0.32	1513, <b>1532</b> , 1543	25	33	*91	Fdi (41), Lw (30), Pw (15), Pli (14)
A_J-NE	0.29	1519, <b>1534</b> , 1550	33	37	*91	Fdi (41), Lw (30), Pw (15), Pli (14)
A_M-NW	1.21	1432, <b>1460</b> , 1498	307	39	216	Hw (50), Cw (30), Bl (20)
A_O-N	1.09	1412, <b>1465</b> , 1513	16	48	6	Cw (30), Hw (20), Lw (20), Pw (20), Fdi (10)
A_O-NE	0.86	1408, <b>1459</b> , 1524	31	57	6	Cw (30), Hw (20), Lw (20), Pw (20), Fdi (10)
A_O-NW	1.20	1421, <b>1454</b> , 1508	316	47	6	Cw (30), Hw (20), Lw (20), Pw (20), Fdi (10)
B_J-E	0.48	1388, <b>1432</b> , 1453	77	49	26	Fdi (40), Sx (30), Pli (20), Lw (10)
B_J-NE	2.06	1368, <b>1408</b> , 1447	46	58	26	Fdi (40), Sx (30), Pli (20), Lw (10)
B_M-E	1.51	1408, <b>1454</b> , 1501	84	40	136	Fdi (70), Lw (20), Cw (10)
B_M-NE	1.60	1455, <b>1485</b> , 1516	56	38	136	Fdi (70), Lw (20), Cw (10)
B_Variable-NE	0.89	1442, <b>1468</b> , 1504	45	70	128	Lw (30), Fdi (25), Bl (15), Pli (10), Cw (10), Se (10)
B_O-E	1.25	1460, <b>1489</b> , 1509	91	31	12	Lw (56), Fdi (22), Pw (13), Pli (9)
B_O-SE	1.10	1455, <b>1483</b> , 1519	122	27	12	Lw (56), Fdi (22), Pw (13), Pli (9)

\* Stand age estimated from the Province of BC historical wildfire database and 1968 historical air photo imagery.



**Table 3** Tree species definitions for species codes recorded in the province of BC Vegetation Resource Inventory and in Table 1.

Species code	Species
Bl	Alpine fir
Cw	Western red cedar
Fdi	Interior Douglas fir
Hw	Western hemlock
Lw	Western larch
Pli	Interior Lodgepole pine
Pw	Western white pine
Se	Engelmann spruce
Sx	Spruce

## TREE SPECIES AND STAND MATURITY

According to the 2022 VRI database, both Site A and Site B exhibit a mix of coniferous species, though their species composition are slightly different.

In Site A, the mature stands are dominated by western hemlock (Hw), western redcedar (Cw), and subalpine fir (Bl), indicative of a moist, late-successional forest type commonly found in cooler, shaded aspects or higher-elevation settings. The juvenile stands contain a mix of Douglas-fir (Fdi), larch (Lw), white pine (Pw), and lodgepole pine (Pli), suggesting more disturbance-driven or transitional conditions. In open areas, species such as cedar (Cw), hemlock (Hw), larch (Lw), white pine (Pw), and Douglas-fir (Fdi) are present.

Site B is more consistently dominated by Douglas-fir (Fdi) across all stand types, possibly reflecting drier conditions. The mature stands contain a mix of Douglas-fir (Fdi), larch (Lw), and western redcedar (Cw), while the juvenile stands include Douglas-fir (Fdi), spruce (Sx), larch (Lw), and lodgepole pine (Pli). In the open stands, larch (Lw) dominates, followed by Douglas-fir (Fdi), white pine (Pw), and lodgepole pine (Pli).

While both sites contain overlapping species such as Douglas-fir and larch, Site A supports a greater presence of shade-tolerant, late-successional species (Hw, Cw, Bl), particularly in mature stands, implying wetter or more sheltered site conditions. In contrast, Site B shows a higher prevalence of early-seral and drought-tolerant species, such as larch, spruce, and pine, pointing to drier conditions, or more solar exposure. These compositional differences are relevant when considering hydrological processes, snow interception, and forest recovery dynamics across the two landscapes.

For Site A, the age ranged from 6 years for the open stands, 91 years for the juvenile stands and 216 years for the mature stand. The age of stands in Site B ranged from 6 years in the open stands to 26 years in the juvenile stands to 136 years in the mature stands. The age recorded in the 2022 VRI for the juvenile stands in Site A did not correspond with in-situ observations of stand maturity. The 91-year age for this juvenile stand was determined using the province of British Columbia's historical wildfire database (<https://maps.gov.bc.ca/ess/hm/imap4m/>) to identify the extent and year of occurrence of an early 1900s wildfire together with a 1968 historical air photo (BC7106-184) downloaded from the province of British Columbia's air photo library (<https://a100.gov.bc.ca/ext/mtec/public/products/airPhoto>) which was used to better delineate the

extent of the fire-disturbed stand and also provided an estimate of the relative height and age of the regenerating stand relative to the adjacent mature stand at that time.

### STAND ELEVATION AND ASPECT

The mean elevation is determined for each stand from the 2014 LiDAR DEM and ranges from 1408 meters for stand B-J-NE to 1534m for stand A-J-NE. All stands include an elevation range of 100 meters or less.

The median (most prevalent) aspect for each study stand is reported in Table 2, however each of these stands have micro-topography which encompasses a broader aspect range. The distribution of slope aspect in degrees within each stand is presented in Figure 3. Degree values corresponding to compass directions are summarized in Table 4.

The greatest slope aspect range is present in stand B-O-SE which includes terrain with east to south aspects while stands A-O-NE and B-J-E display the most limited slope aspect range.

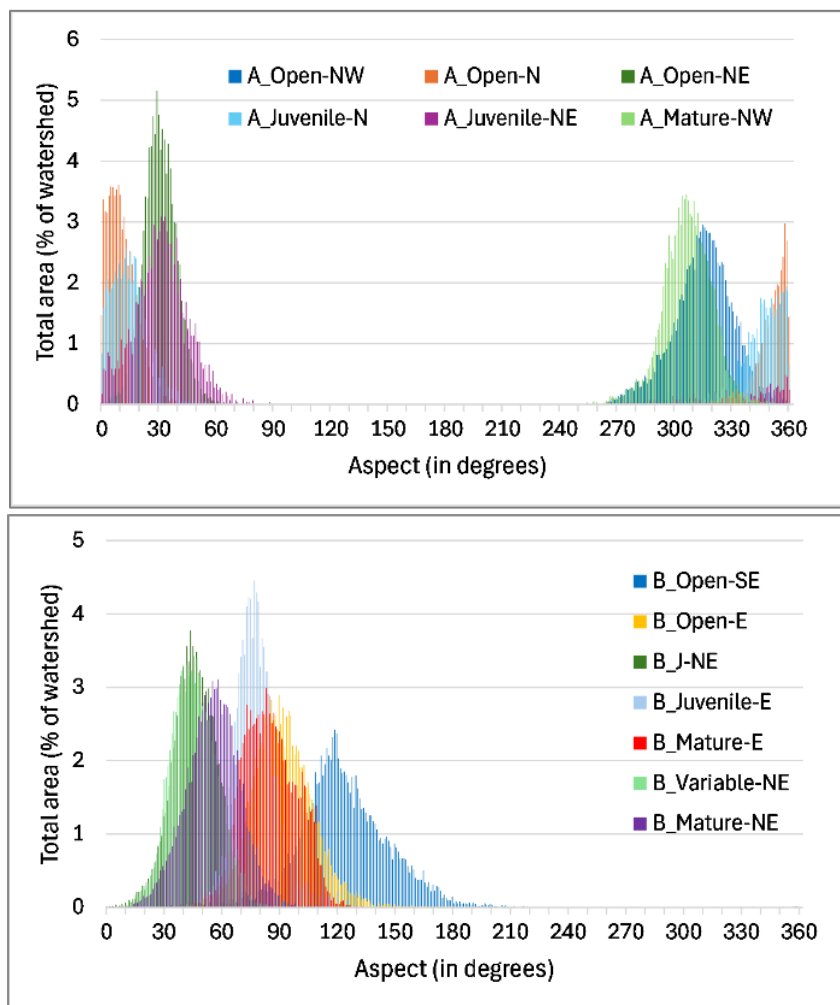


**Figure 3** Aspect distributions for stands in study sites A (top) and B (bottom).

*Table 4 Slope aspect according to aspect ranges in degrees.*

Aspect range (in degrees)	Assigned aspect
0 - 22.5	North
22.5 - 67.5	Northeast
67.5 - 112.5	East
112.5 - 157.5	Southeast
157.5 - 202.5	South
202.5 - 247.5	Southwest
247.5 - 292.5	West
292.5 - 337.5	Northwest
337.5 - 360	North

## SLOPE GRADIENT BY STAND

Mean slope gradients ranged from 33% to 57% for the stands in Site A and 27% to 70% for the stands in Site B (Table 2).

## 2.0 Methods

### 2.1 Field Data Collection

UAV–LiDAR scans were collected approximately weekly (depending on the weather) from March 25 through June 16, 2022, encompassing the period of peak snow accumulation and the duration of the melt season. Aerial scans were collected using a Zenmuse L1-DJ1 scanner which has a detection range of 450 meters at 80% reflectivity, a single point return rate 240,000 pts/s, and an accuracy of 10 cm horizontal and 5 cm vertical with a final accuracy after correction of 8.0 cm (z), 1.3 cm (y), 1.6 cm (x).

### 2.2 Data Processing

#### LIDAR

The software and processing hardware available to Selkirk Innovates allows for efficient LiDAR data processing. The list of applications used in this project from which point-cloud data and orthomosaic imagery products were processed is provided in Appendix 1. The workflow used to generate useable data from the raw LiDAR data files is outlined here.

#### LIDAR PROCESSING PIPELINE

To manage the high volume of LiDAR data, a coded pipeline was used to reduce error while processing numerous point clouds at once to create outputs including DTMs, Canopy Height Models (CHM), snow depth, and SWE. The term “pipeline” is used here to describe the automated process of feeding multiple files through lines of code that result in various outputs, which are then used to determine melt rates and SWE to compare between stands. The pipeline used LAStools (Isenburg, 2022), PDAL (PDAL

Contributors, 2022) and LidR (Rousell and Auty, 2022) software applications for ground classification, normalized height and canopy height determination. Using a coded pipeline to loop through hundreds of files is far more efficient compared to manually processing each point cloud.

Aerial point clouds were initially corrected, pre-processed and georectified using Phoenix LiDAR Systems Spatial Explorer and DGI Terra to achieve a final accuracy after correction of 8.0 cm (z), 1.3 cm (y), 1.6 cm (x). Individual, georeferenced LiDAR point clouds resulting from all LiDAR scans in each site were co-registered in CloudCompare (CloudCompare, 2022) to improve relative alignment between individual LiDAR scans collected within each site.

#### LIDAR POINT CLOUD CO-REGISTRATION

To obtain a comparable time-series of snow depths for each forest stand included in the project the point clouds obtained from the post-processed L1-DJ1 scanner needed to be aligned (co-registered) to a single date (base file) so that the changes in snow depth between scans could be accurately measured. Precise alignment of the series of point clouds was facilitated using checkerboard ground control points (GCP) distributed through the flight area (Figures 4A, B and C).

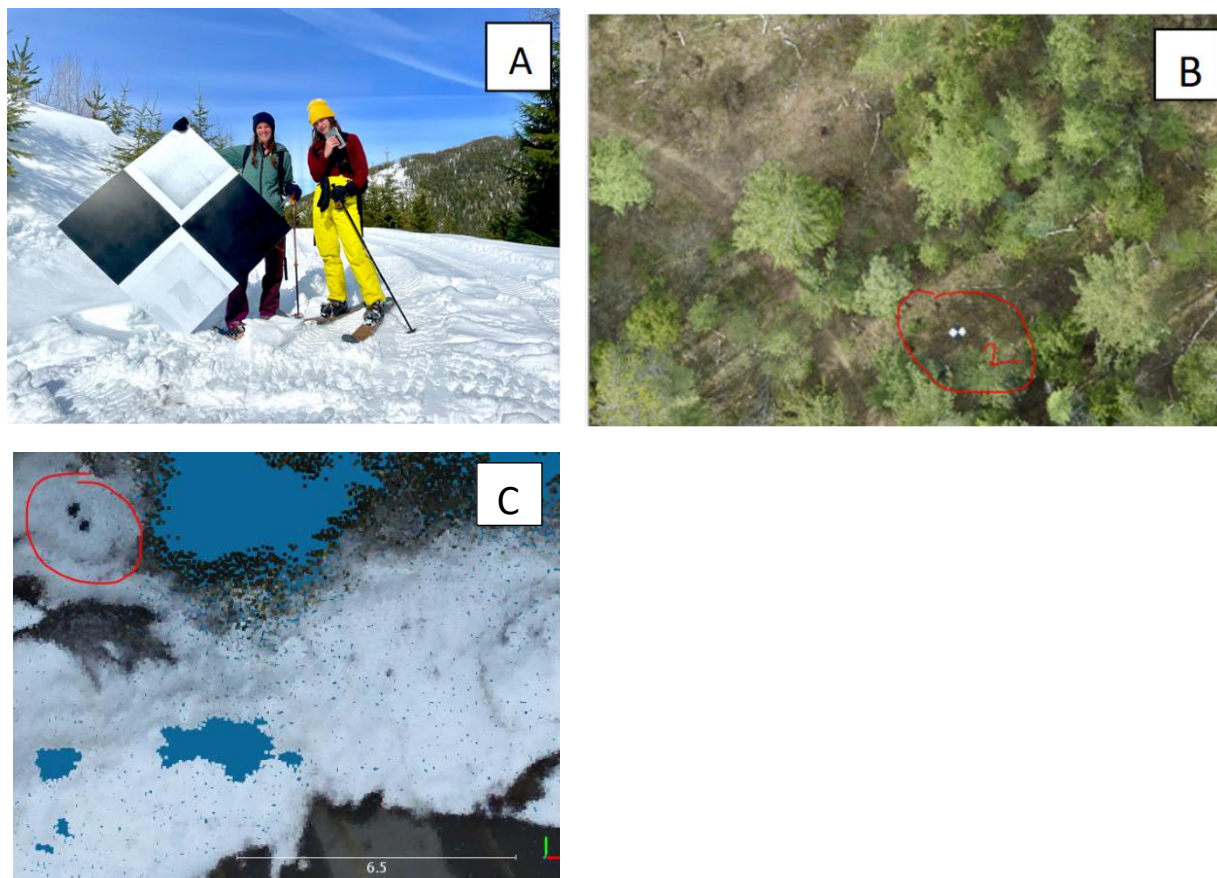


**Figure 4.** 1-meter square (A) Checkerboard targets distributed through the flight area (B) allowed for alignment of multiple LiDAR point clouds taken over the snow melt period. Image C shows the visibility of the checkerboard in the LiDAR point cloud.



## GROUND SURFACE AND SNOW SURFACE MODEL CREATION

Digital terrain models (DTMs) of the ground and snow surface models were produced by filtering and thinning the post-processed .las files to select the points representative of ground surface and snow surface returns. The point clouds were further filtered to remove outliers that may represent vegetation influences and to derive the smoothest possible surface elevation model. The resulting point clouds used to generate the DTMs and snow surface models were inspected visually to ensure they are reasonably representative of the snow surface. Particular attention was paid to potential bridging artifacts, which can occur in areas with sparse ground returns and result in over-interpolated terrain surfaces and vegetation pop-up effects as under canopy brush shed snow in the later spring scans. We determined that the point clouds had sufficient ground point density and minimal bridging, providing confidence in the reliability of the derived DTMs.

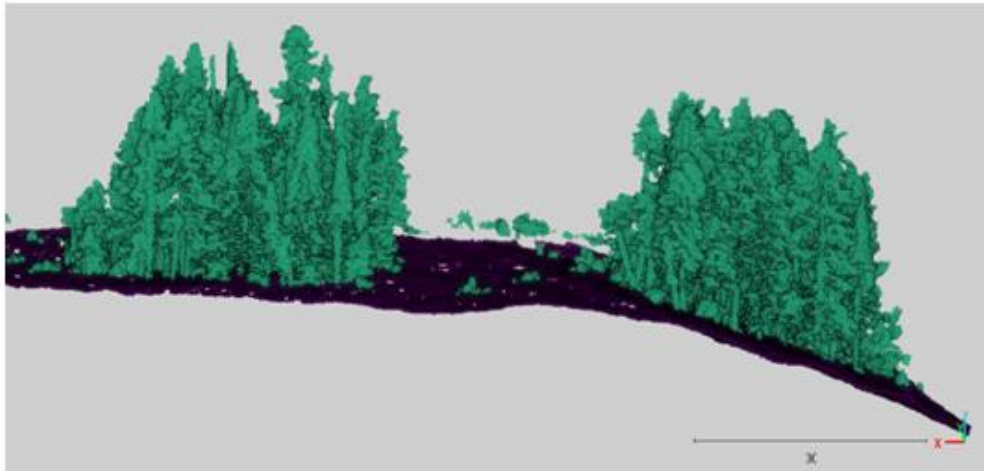


Figure 5. Example of ground classified point cloud. Black highlights the elevation model of the ground surface.

## SNOW DEPTH RASTER CREATION

An area of interest (AOI) was used to clip DTMs to overlapping high point density areas to avoid edge effects. The snow free DTMs were subtracted from all other scans to determine snow depth.

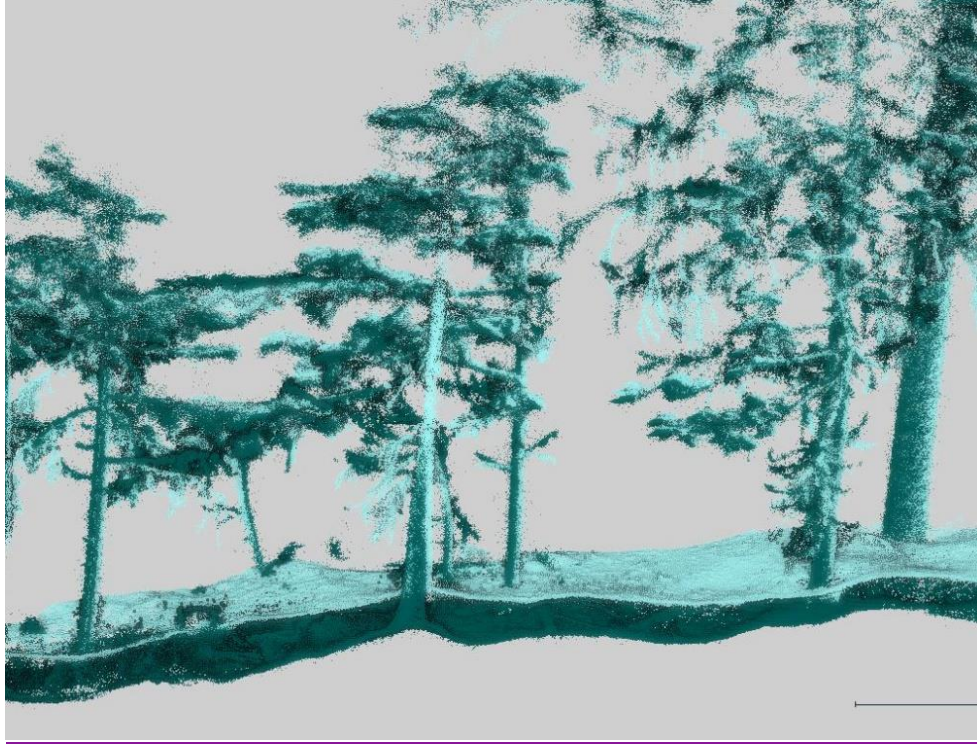


Figure 6. Two aligned L1 point clouds showing the change in snow surface between dates.

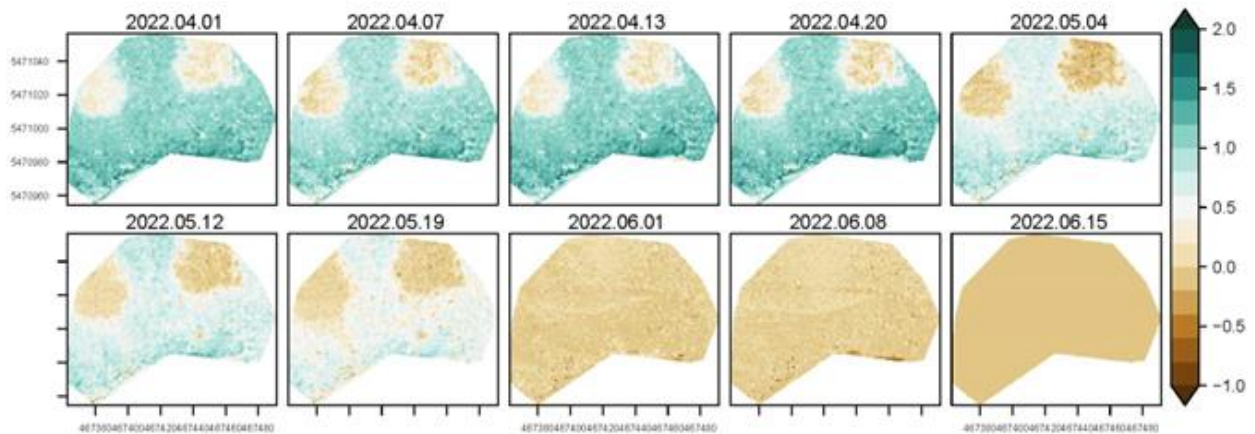


Figure 7. Snow depth rasters (in meters) over time for Site A (open stand) created by subtracting ground surface elevation from snow surface elevation for each raster grid point.

## FOREST STAND METRICS

Forest stand height and canopy cover metrics for each stand considered in sites A and B were determined using the resulting CHMs developed for each site. Individual treetop heights and tree crown extents were derived using a publicly available treetop delineation software (Skelly, 2020). This software, which uses an iterative process to delineate tree crowns within variable-height stands, was

found to outperform tree delineation tools available in either the rLiDAR or lidR software packages in R by more accurately identifying the crown extents of smaller trees. For each site, stand metrics including tree count, tree height (average, median, minimum, and maximum), tree height standard deviation, and crown cover % for trees greater than 2 min height were determined. The 2-meter height threshold was chosen based on in-situ observations of sub-canopy ground vegetation characteristics and aims to reduce the influence of ground vegetation on stand height or crown cover metrics determined for the stand.

## CALCULATING SWE FROM SNOW DEPTH

Information on snow density, which is a measure of the saturation of the snowpack, is needed to convert snow depth to SWE (Equation 1).

$$SWE(mm) = \sum \left[ \text{Vertical Thickness of snowpack (cm)} * \text{Density} \left( \frac{kg}{m^3} \right) \right] * 0.01 \text{ (Eq 1. CAA, 2016)}$$

Snow density values were not collected at the field site during the 2022 data collection period. To calculate SWE for the 2022 season we explored several methods of estimating snow density at the field site at the time of the LiDAR data collection using regional snow survey data collected at nearby sites.

The approaches applied to investigate SWE estimation ranged from using simple interpolation techniques to complex statistical models combined with polynomial regression to address the intricacies of snow density, snow water equivalent (SWE), and snow depth (Appendix 2). Of the methods explored, the application of the linear regressions between snow depth and SWE developed for the same sites during the 2020 snow melt period was determined to be the best approach for estimating SWE from the 2022 snow depths. snow density at each site. The linear model approach offered a clear advantage in that it assumes a direct positive relationship between snow depth and SWE, simplifying the process of estimation and interpretation and avoiding the limitations that came with more complex approaches or calendar-based assumptions.

Prior to the application of the linear models, the 2020 meteorology for the Rover sites were investigated and it was determined that these conditions (i.e., trends in 3-day mean temperature) reasonably applied to the 2022 snowmelt period (Figure 8).

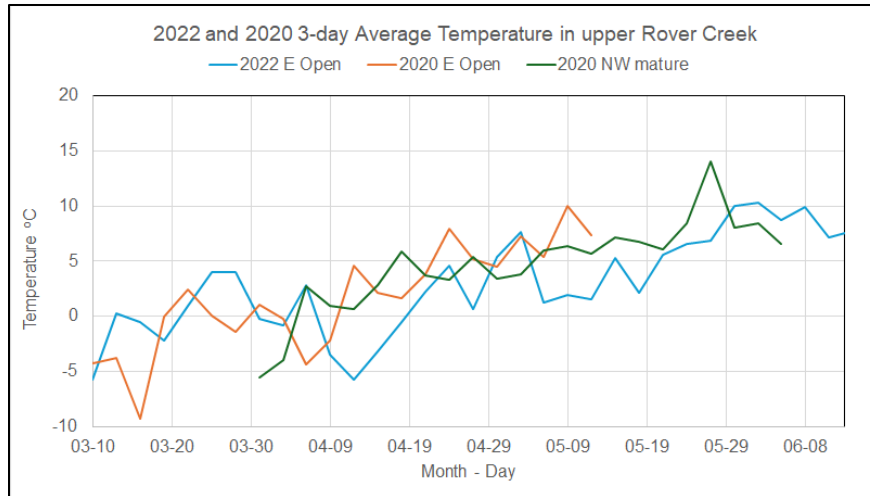


Figure 8. Comparison of 3-day average temperatures for two 2020 temperature monitoring sites with the 2022 East Open site.

Data cleaning involved assessing the 2020 dataset for outlying data points, assessing the snow core data for accuracy, completeness and any missing data. Missing data points (noted as 0's) were omitted from the analysis as these values would affect the underlying structure and bring down the averages of the depth and therefore result in lower site-averaged SWE values.

The resulting linear models developed for each site are show in Table 5. Applying these models to the 2022 data results in the greatest uncertainty in calculated SWE at the start of the data collection period (i.e., late March and early April) prior to the settling and saturation of the snowpack.

Table 5. Linear models applied to 2022 snow depth data.

Site	Linear Model	R <sup>2</sup>
A-Open	$SWE(mm) = (0.360 * Depth(cm)) + 1.772$	0.97
A-Mature	$SWE(mm) = (0.3487 * Depth(cm)) + 1.2302$	0.99
B-Open	$SWE(mm) = (0.435 * Depth(cm)) + 0.2939$	0.99
B-Juvenile	$SWE(mm) = (0.3631 * Depth(cm)) + 0.6526$	0.99
B-Mature	$SWE(mm) = (0.367 * Depth(cm)) + 0.4778$	0.98

For SWE values ranging from 50mm to less than 5mm, representative of the peak to nearly snow free period, the corresponding snow density according to the models ranges from between 36% to 53% with the highest range of snow density found in the north aspect open stand of Site A and the lowest range found in the southeast aspect open stand of Site B (Figure 9). This range in snow density represents the maturing snowpack through the snowmelt period.



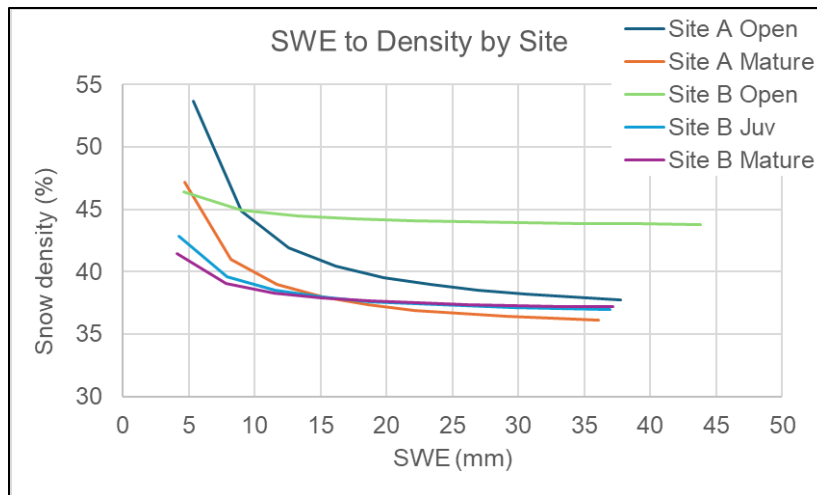


Figure 9. Linear models between snow depth and SWE applied to the 2022 snow depth data.

For Site A- J, where observations of snow depth to SWE was lacking for 2020, we extrapolated using the equation from the most similar stand (Stand A-M), ensuring consistency across our analysis.

#### Converting Snow Depth Rasters to SWE Rasters

Once the snow water equivalent to snow depth regression equations were determined for each stand (Table 5) they were applied to each snow depth raster to create the SWE rasters. Snow depth raster files were loaded into R, then a mask was applied to each merged snow depth raster file to define the spatial extent of each stand. New raster files for each stand were created by applying a snow depth value (represented within each pixel of the snow depth raster) to the snow depth to SWE model. This created a new raster file for each stand representing the SWE values. Once all stands were converted into raster files, a merged file was then created for Sites A and B showing SWE for the entire study area for each day of LiDAR scans.

### **ANALYSIS METHODS**

#### Peak SWE

Boxplots were created from the SWE rasters for a sample date deemed to best represent peak SWE using the 12.5% quartile and 87% quartile to plot 75% of the dataset. By limiting the data analysis to the central 75% of raster points we excluded outlying data points that were likely created due to improper alignment of the .las files as well as artifacts in snow depth caused by low lying vegetation and forest floor debris rebounding as the snow melted. The peak SWE day was selected as April 20<sup>th</sup> to avoid greater uncertainty in the depth to SWE relationship for the earliest dates in the snowmelt period. Boxplots were created for groupings of Sites and stand maturity (ex. Mature stands for both Site A and Site B were plotted together) to compare how SWE was affected by both stand maturity and aspect.

#### Ablation Rate Calculations

A consistent ablation period was selected for all stands based on the timing of peak SWE, the LiDAR scan dates and the start of snow free conditions. A period of 29 days was decided on due to the scan dates

available on April 20<sup>th</sup> for peak SWE, and May 19<sup>th</sup> for the end of the ablation period corresponding to the steepest decline in SWE. Based on the selected dates, we calculated ablation rates through the following equation where the number of days was equal to 30 including end-dates.

$$\text{Daily Ablation Rate} = \frac{(\text{Max SWE} - \text{Min SWE})}{\text{Number of Days}} \quad (\text{Eq. 2})$$

Using this method, we were able to compare and contrast ablation rates for all stands in Sites A and B revealing differences stemming from different aspects and stand maturity.

#### Hydrological Recovery calculations

Hydrological recovery describes the restoration of hydrological process of snow accumulation (i.e., peak SWE) and ablation to pre-disturbance conditions. Hydrological recovery is expressed as 0% for clearcut and 100% for a regenerated mature stand (Winkler and Boon, 2015) and is calculated as a percentage relative to the clearcut and mature forest values according to the following equation.

$$SR = \left[ \frac{(Sc - Sy)}{(Sc - Sm)} \right] * 100\% \quad (\text{Eq. 3})$$

Where SR describes the percent (%) snow recovery for the variables of interest; peak SWE (cm) or ablation rate (cm/day) for the stand-averaged snowpack (Sy) compared to an average index value of each variable measured for the clearcut condition (Sc) and the mature stand (Sm).

#### Statistical Analysis of SWE and Ablation Rasters

The SWE and ablation rasters were investigated for normality of the data distribution by plotting the histograms for each raster to visually investigate the shape of the distributions and by using Q – Q plots. A Q-Q plot or quantile – quantile plot is created by plotting the theoretical quantiles from normally distributed data against the observed data quantiles. Normally distributed or nearly normally distributed data will follow a linear relationship with the theoretical normally distributed data.

Due to the very large sample size of the SWE and ablation rasters, traditional tests of statistical significance for similarities/differences in stand-level peak SWE and ablation rates are not appropriate. For very large samples, P-values will always be very small so the test will always result in significant differences between samples (Khalilzadeh and Tasci, 2017). To determine if peak SWE or ablation rates are similar or different between stands, the effect size or practical significance is determined using Cohen's d which is insensitive to sample size. Cohen's d is calculated according to the following equation.

$$d = \frac{\mu_1 - \mu_2}{\sigma} \quad (\text{Eq. 4})$$

In which  $\mu_1$  and  $\mu_2$  are the mean values for groups 1 and 2 respectively and  $\sigma$  is the control group standard deviation. The difference is always greater than zero. Effect size thresholds (i.e. whether the treatment is substantially different than the control condition) based on Cohen's d values are provided in Table 6.

**Table 6.** Effect size thresholds for practical significance of differences between rasters.

Effect size (Cohen's d)	Practical Significance
0 – 0.2	No substantial difference
0.21 – 0.5	Modest difference
0.51 – 0.8	Moderate difference
>0.8	Large difference

## 3.0 Results

### 3.1 LiDAR-derived forest stand metrics

LiDAR derived forest stand metrics for Sites A and B are included in Table 7. Site A median stand heights range from 3 meters in the open stands to over 37 meters in the mature stand while crown cover ranges from 7% in the open stands to over 97% in the mature stand. Site B stand metrics include similar median height ranges (3.2m to 35m) but the crown cover values for the open stands are higher (25% and 34%). Juvenile stands in Site A are more advanced in growth (median height of 23.7m and 25.7m) compared to the juvenile stands of site B (median height of 10m) but the crown cover is higher in Site B juvenile stands (96%) compared to Site A (89% and 91%). The 'Variable' stand in Site B is unique in that it includes both mature and early juvenile trees consistent with a partial retention (~60%) cutblock or beetle-killed stand.

**Table 7** Site-specific stand metrics organized by stand and aspect. Information here includes the following: tree count; trees per hectare; average, median, minimum, and maximum tree height (m); standard deviation in tree height (m); and crown cover (%).

Stand	Tree count	Trees per hectare	Average ht (m)	Median ht (m)	Minimum ht (m)	Maximum ht (m)	St.Dev. ht (m)	Crown cover (%)
A_J-N	109	339	25.7	26.6	11.1	36.0	5.0	91.4
A_J-NE	93	319	23.7	24.3	6.6	33.2	4.5	89.4
A_M-NW	283	233	37.7	38.3	17.9	48.5	4.5	97.4
A_O-N	492	453	3.0	2.8	1.6	30.3	1.6	14.4
A_O-NE	630	733	3.0	2.9	1.7	8.4	0.9	25.7
A_O-NW	249	208	3.1	2.6	1.6	34.1	2.5	7.0
B_J-E	311	644	10.0	10.0	5.7	13.6	1.2	96.0
B_J-NE	1405	680	10.2	10.2	3.7	16.8	1.5	96.6
B_M-E	382	252	35.0	35.6	17.0	45.4	5.1	96.0
B_M-NE	410	256	33.4	35.4	13.4	44.4	6.8	93.5
B_Variable-NE	329	371	9.5	6.7	1.7	37.3	7.9	62.2
B_O-E	694	556	3.2	2.9	1.7	31.7	1.6	25.1
B_O-SE	595	540	3.5	3.2	1.8	31.7	1.7	34.3

### 3.2 Trends in peak SWE and ablation rates from LiDAR-derived snow depth

#### 3.2.1 TRENDS IN MEDIAN SWE OVER TIME

Figure 10 shows the median SWE values for all stands in Sites A and B over the study period from March 25<sup>th</sup>, 2022, until June 18<sup>th</sup>, 2022, with stands in both sites at or approaching 0 SWE by the final scan date of June 18<sup>th</sup>, 2022. The grey box in both figures identifies the date period selected to represent peak SWE and the ablation period to facilitate comparisons across sites.

Each stand in Site A (Figure 10, top panel) shows a unique trajectory of SWE decline through the spring snowmelt period. The highest initial SWE was recorded in the open stands, while the lowest was observed in the juvenile stands. Parallel SWE trends were observed in the open stands across the sampling period although median SWE values are lower in the NE stand compared to the N and NW stands. SWE levels plateaued for all stands in Site A during mid-April in response to a period of cooler temperatures (Figure 8) but decreased rapidly starting at the end of April. The mature stand in Site A consistently had the lowest SWE values from early April onwards and a slower decrease in SWE through the latter half of the study period. The two juvenile stands recorded nearly identical median SWE values through the study period and were the first to be snow-free by the June 1<sup>st</sup> scan. Site A open stands showed an increase in SWE after the start of the melt period, a behavior not observed in either the juvenile or mature Site A stands. Open stands experienced the fastest and largest decrease in SWE during the comparison period, while mature stands had the slowest decline in SWE. The advanced juvenile stands (A-J-N and A-J-NE) showed SWE trends more like mature stands than open stands.

Median SWE trends in Site B (Figure 10, lower panel) varied substantially across stands during the early portion of the study period but all stands displayed similar patterns in SWE decreases during the April 20<sup>th</sup> to May 19<sup>th</sup> comparison period. The open east stand (B-O-E) had the highest initial SWE values, while the mature northeast and east stands (B-M-NE, B-M-E) recorded the lowest. Open stands were the first to become snow-free, followed by juvenile stands, with mature stands retaining snow the longest. During the April 20<sup>th</sup> to May 19<sup>th</sup> comparison period, the juvenile east aspect stand (B-J-E) experienced the largest decrease in SWE. The two juvenile stands displayed distinctly different trends in SWE depletion during the comparison period despite their adjacency and similarities in stand characteristics. The mature variable stand (B-M-VAR) behaved more like an open stand, with a steeper decrease in SWE compared to other mature stands. The open southeast stand (B-O-SE) ended the study period with the lowest SWE and exhibited the greatest decrease in SWE during the comparison period among all stands in Site B.



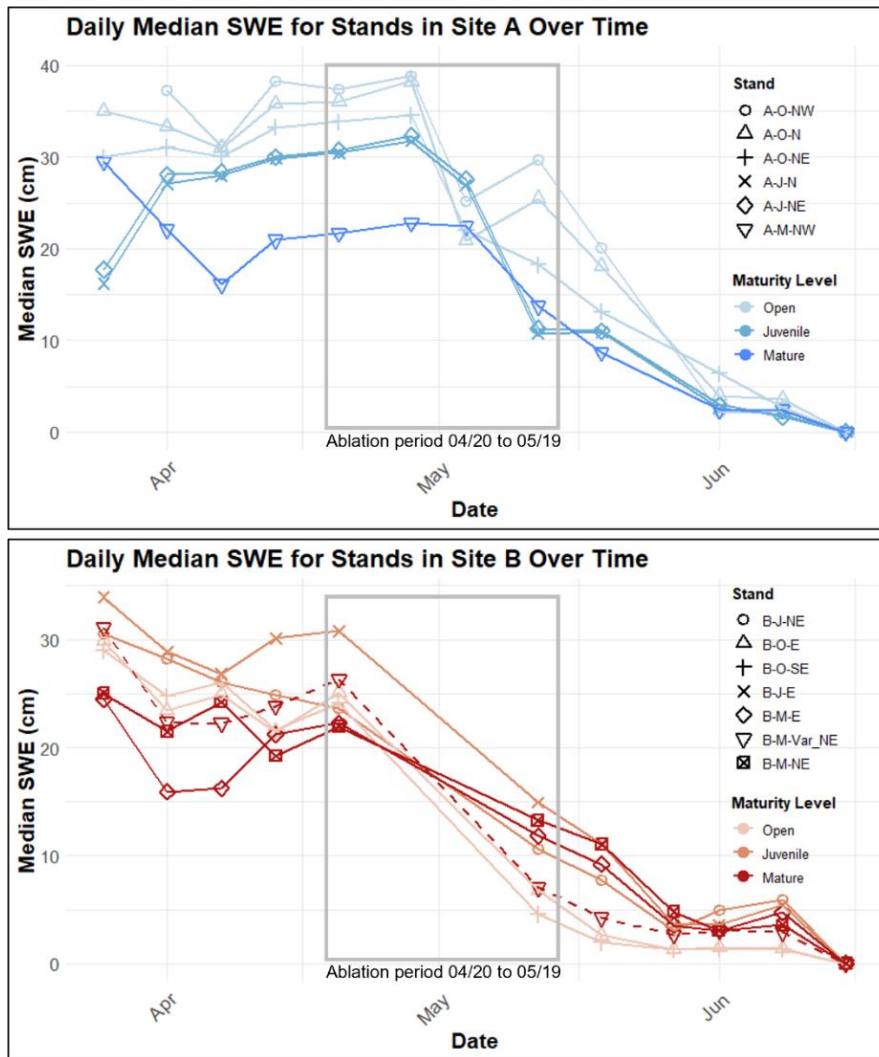


Figure 10. Median SWE over time for all stands in Site A (top) and Site B (bottom). The median SWE trend over time for the variable retention mature stand of Site B is indicated with the dashed line.

By June 1<sup>st</sup>, SWE in all stands in Sites A and B approached zero, but juvenile and mature stands in Site B (E and NE aspects) retained snow patches longer into the melt season than open stands (E and SE aspects), contrasting with the earlier snow-free status of the advanced juvenile (N and NE aspects) and mature (NW aspects) stands of Site A relative to the open stands in Site A (NW to NE aspects). The apparent elevation of median SWE in the juvenile and mature stands of Site B beyond June 1<sup>st</sup> is due to the presence of sub-canopy brush confounding ground classification in these snow free scans.

There is limited published research available to compare the site-level and stand-level SWE trends observed at Rover Creek. The slower SWE disappearance in the northwest, north and northeast open stands relative to the northwest forest stand of Site A is consistent with studies of northern aspect open – forest stand pairs from sites in the Columbia and Rocky Mountains (Jost et al., 2007; Ellis et al., 2011) and is also consistent with the observed pattern of snow disappearance from Rover Creek north to northeast aspect lower elevation stands reported in Potter and others (2024). The observed pattern of

earlier snow disappearance from southeast and east open stands compared to adjacent northeast and east forest stands observed at Site B is also generally consistent with the SWE disappearance patterns reported for south and west aspect open and forested stands reported in Jost and others (2007) and Ellis and others (2011). The SWE trends observed in the juvenile east through northeast stands of Site A and B have no counterparts in published literature to compare with. The rapid SWE depletion trend observed in the variable retention northeast mature stand of Site B is more consistent to the SWE trend observed for a mechanically thinned south-aspect stand than the trend observed for a thinned north aspect stand in the east slopes Rocky Mountains (Ellis et al., 2013). In the Rocky Mountain study, the timing/rate of SWE depletion is closely linked to the daily melt energy which is dominated by the combined net shortwave and longwave radiation at the snow surface.

### 3.2.2 COMPARING PEAK SWE WITHIN AND ACROSS SITES.

Boxplots constructed using the 12.5% and 87.5% quartile values for April 20<sup>th</sup> allow for a visual comparison of median peak SWE and SWE variability across all stands (Figure 11). SWE values in each raster beyond these quartile ranges were removed to reduce processing artifacts (specifically negative values) from skewing the results. Table 8 shows the mean and median peak SWE and standard deviation for all stands.

*Table 8. Peak SWE by stand*

Stand	April 20 Peak SWE (cm)		
	Mean	Median	SD
<b>A-O-NW</b>	37.2	37.4	8.7
<b>A-O-N</b>	34.5	36	10.9
<b>A-O-NE</b>	33.8	34	13.7
<b>A-J-N</b>	30.7	30.4	8.0
<b>A-J-NE</b>	31.3	30.8	8.1
<b>A-M-NW</b>	21.5	21.7	6.6
<b>B-O-E</b>	25.0	25.1	6.6
<b>B-O-SE</b>	23.8	24.2	8.1
<b>B-J-E</b>	30.6	30.8	9.1
<b>B-J-NE</b>	23.7	23.7	8.7
<b>B-M-E</b>	22.5	22.3	6.9
<b>B-M-NE</b>	22.1	21.9	7.0
<b>B-M-Var-NE</b>	25.8	26.6	10.7

This study shows that peak SWE was higher in the northwest, north and northeast open stands of Site A than in the southeast and east open stands of Site B (Figure 11). Additionally, the broader box plots indicate the standard deviation in peak SWE for the open stands was greater in Site A than in Site B (Table 8). A comparison of juvenile stands across sites shows differences in peak SWE associated with stand structure and aspect. Site A north and northeast aspect advanced juvenile (25m height) stands recorded nearly identical median peak SWE and SWE variability while less advanced (10m) northeast and east-aspect stands in Site B displayed different median SWE values and larger standard deviations compared to Site A. The mature stands of Site A (northwest aspect) and Site B (northeast and east aspect) displayed similar median and standard deviation but the mature variable retention northeast aspect stand of Site B displayed a higher peak SWE with a much larger standard deviation.

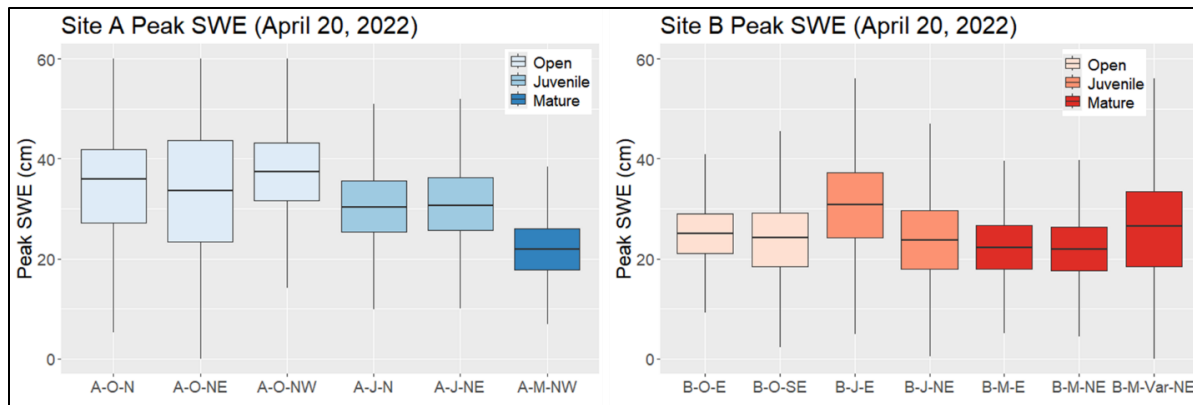


Figure 11. Median and 3 standard deviation range in Peak SWE comparison across Sites A and B

Based on the Q-Q plots most peak SWE rasters displayed normal or nearly normal distributions which are illustrated in plots of the raster histograms and Q – Q plots included in Appendix 3.

The Cohen’s d test for practical significance indicates that within Site A open stands display no difference or modest differences in Peak SWE for aspects ranging from NW to NE, while juvenile stands that range from N to NE display no significant differences in peak SWE. Small to modest differences are also observed between the open and juvenile stands of Site A, however, large differences in peak SWE are indicated between all open stands and the mature stand of Site A and between both juvenile stand and the mature stand of Site A.

The Cohen’s d test applied to Site B stands indicates no significant differences in peak SWE for open East and Southeast stands or between mature northeast and east stands (Table 11, Appendix 3). Moderate differences are indicated between juvenile stands peak SWE. Open and mature stands record modest differences in peak SWE while only the juvenile east aspect stand shows large differences in peak SWE compared to the mature stands. In contrast, the northeast aspect juvenile stand of Site B shows no statistically significant difference in peak SWE compared to the mature stands.

No significant differences in peak SWE are confirmed between Site A and Site B mature stands which range in aspect from NW to E and NE (excluding the mature variable site) while peak SWE in open stands across sites show large differences.

The observations of higher median peak SWE for north aspect open stands are consistent with those observed for contrasting north and south aspect open stands in the Rocky Mountains (Marmot Basin) reported by Ellis and others (2011) where they found greater SWE in the north aspect open stand than in a nearby south aspect open stand for spruce-leading stands above 2000 meters elevation. Ellis and others (2011) also reported no differences in SWE for the forested sites with contrasting aspects. Ellis and others (2011) related these outcomes to the energy balance at the snow surface. They determined that beneath the mature canopy the snowpack was exposed to nearly identical daily net radiation throughout the study period. However, the south aspect open stand experienced higher net radiation relative to the north aspect open stand from approximately mid-April onwards in the Rocky Mountain study area. The decreased SWE variability observed with increasing juvenile stand maturity was

reported by Potter and others (2024) for the stands in lower Rover Creek which was determined to be due to the increased canopy interception capacity in the more mature juvenile stand.

#### COMPARISON OF ABLATION RATES FOR THE APRIL 20<sup>TH</sup> TO MAY 19<sup>TH</sup> PERIOD

Box plots are used to compare median daily ablation rates for all stands in Sites A (blue) and B (red) from April 20, 2022, to May 19, 2022 (Figure 12). Table 9 shows the mean and median ablation rates and standard deviation values for all stands.

*Table 9. April 20 to May 19<sup>th</sup> ablation rates for all stands.*

Stand	April 20 to May 19 ablation rate (cm/day)		
	Mean	Median	SD
<b>A-O-NW</b>	0.59	0.57	0.15
<b>A-O-N</b>	0.59	0.57	0.18
<b>A-O-NE</b>	0.77	0.76	0.24
<b>A-J-N</b>	0.65	0.64	0.14
<b>A-J-NE</b>	0.66	0.65	0.16
<b>A-M-NW</b>	0.43	0.44	0.17
<b>B-O-E</b>	0.78	0.79	0.16
<b>B-O-SE</b>	0.80	0.84	0.20
<b>B-J-E</b>	0.64	0.64	0.18
<b>B-J-NE</b>	0.52	0.53	0.25
<b>B-M-E</b>	0.44	0.43	0.17
<b>B-M-NE</b>	0.37	0.36	0.16
<b>B-M-Var-NE</b>	0.74	0.82	0.38

For the selected period, the stands with the highest median ablation rates were the open stands of Site B with the open southeast stand (B-O-SE) recording a period-averaged median ablation rate of 0.84 cm/day and the adjacent open east stand (B-O-E) recording a nearly identical averaged ablation rate of 0.79 cm/day. Open stands of Site A showed notably lower median ablation rates ranging from 0.57 cm/day in the open NW and N stands up to 0.76 cm/day in the open NE stand. Juvenile stands from both Sites A and B recorded similar ablation rates that ranged from 0.64 to 0.65 cm/day in the advanced juvenile (i.e. 25m) stand of Site A and from 0.53 to 0.64 cm/day in the less advanced (10m) juvenile sites in Site B. The mature stands in both Site A and Site B, with aspects ranging from east and northeast (Site B) to northwest (Site A), recorded the lowest median ablation rates of 0.36 cm/day to 0.44 cm/day. The variable retention mature stand of Site B (B-M-Var-NE) recorded second highest ablation rate (0.82 cm/day) and the highest standard deviation of all stands.



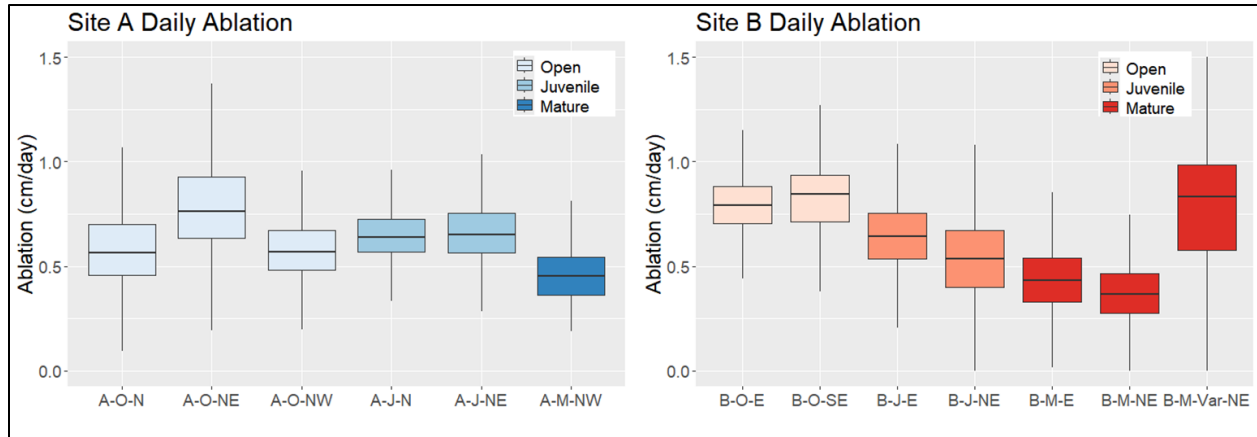


Figure 12. Boxplot comparison of median daily ablation rates for all stands in the study area for the selected period spanning 29 days between April 20<sup>th</sup>, and May 19<sup>th</sup>, 2022.

Cohen's d tests of practical significance of the differences between mean ablation rates for Site A indicate no difference in open north and northwest ablation rates but a moderate difference in ablation rate for the northeast open stand. There is also no significant difference in ablation rate for the two advanced juvenile stands of Site A. For Site B, no statistical differences exist between the east and southeast open stands of Site B or between the northeast and east mature stands of Site B. Moderate differences in ablation rate are found between the two juvenile (east and northeast) stands of Site B. Across Sites, the mature stands A-M-NW and B-M-E show no significant difference in ablation rates with mature site B-M-NE showing only a modest difference in ablation from the other two mature sites (Table 12, Appendix 3). The B-M-Var stand of Site B displays an ablation rate that is similar to the open NE stand of site A and the open E and SE stands of Site B.

There are no published studies with which to compare ablation rates for differing forest maturity and aspect conditions. Jost and others (2007) did not explicitly investigate snowmelt differences across aspects for different forest maturity conditions however they did demonstrate that forest cover and aspect are the primary controls on SWE behavior during the spring period and surmise that this is due to the influence of these factors on below canopy/snow surface air temperature which is driving snowmelt during the April through May period. Winkler and others (2005) demonstrated that in flat terrain increasing forest maturity contributed to decreasing ablation rates which was linked to decreasing net radiation at the snow surface. Ellis and others (2013) investigated canopy thinning effects on snowmelt timing and determined that slope aspect plays a key role on timing of snowmelt. They determined that north aspect thinned stands result in a delay in snowmelt relative to the fully forested stand while south aspect thinning results in an advance in the timing of snowmelt relative to the forested stand. As with other studies, Ellis and others were able to link the differences between forest and thinned stand snowmelt timing to the energy balance at the snow surface.

### 3.2.3 CHARACTERIZING ASPECT AND FOREST MATURITY INFLUENCES ON PEAK SWE AND ABLATION RATES

Trends in median peak SWE and ablation rate with tree height are investigated for stands in both Site A and Site B. The difference in both peak SWE and ablation rate are measured relative to the mature stands.

### PEAK SWE WITH TREE HEIGHT

An investigation of trends in median peak SWE with median stand height shows that peak SWE generally decreased with increasing tree height for both Site A and Site B (Figure 13). The visual trends present in Figure 13 suggests a steeper decrease in peak SWE with increasing tree height for Site A compared to Site B suggesting different peak SWE recovery relationships for different aspects. The juvenile east stand (B-J-E), which displayed a higher peak SWE than both the open site and the adjacent juvenile site, appears to be an outlier to the trend for Site B.

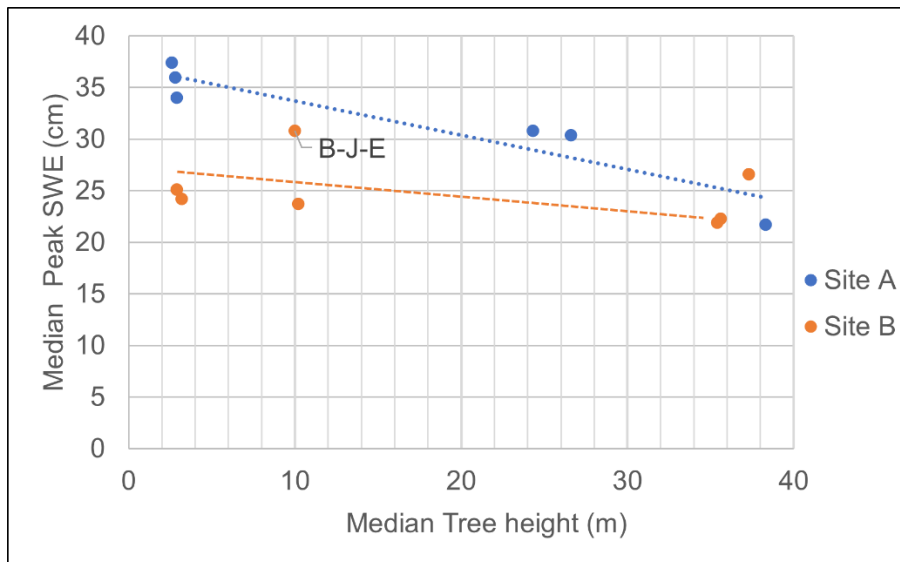


Figure 13. Trends in stand median peak SWE with median tree height.

Aspect related differences in the relationships between peak SWE and median stand height have not been previously reported but the general trend of decreasing SWE with increasing tree height is consistent previous studies of forest maturity effects on peak SWE from gentle terrain study sites in central and southern BC (Winkler, 2001; Jost et al., 2007; Winkler et al., 2010). Winkler (2001) established that crown height, which is closely represented by tree height, is the primary control on snow interception capacity of a forest stand. Both Jost and others (2007) and Winkler and others (2010) link forest maturity and the below canopy total net energy balance (where total net energy is the sum of the incoming short wave and longwave radiation acting on the snow surface and, to a lesser extent, the contributions from latent and sensible heat fluxes) to the trend of decreasing peak SWE with increasing stand height. The deviation from the trend at B-J-E may be due to localized topographic and/or shading effects that were not controlled for in this study design. Potter and others (2024), Winkler and Moore (2006) and Jost and others (2007) all found that micro-topographic effects have a substantial bearing on peak SWE distribution across a forest stand. The similarity in peak SWE for mature forested stands at similar elevations with differing aspects (north and south) was reported by Ellis and others (2011) for study sites on the east slopes of the Rocky Mountains and is attributed to similar total net longwave and shortwave energy beneath the mature canopies throughout the accumulation and melt periods.

#### ABLATION RATE TRENDS WITH TREE HEIGHT

Trends for April 20<sup>th</sup> to May 19<sup>th</sup> daily average ablation rate with median stand height are inconsistent between Sites A and B (Figure 14).

At Site A both the open and juvenile stand median ablation rates were higher than the ablation rate recorded in the adjacent mature stand however, the ablation rates for the juvenile stands in Site A are similar to the open stands resulting in a substantial delay in the change in the ablation rate with increasing stand height for this site. In contrast, there was a clear decrease in ablation rate observed between open and juvenile stands of Site B and a further decrease in ablation rate between juvenile and mature stands. The mature-variable retention stand (B-M-Var-NE) is an outlier to the trend for Site B with an ablation rate higher than either juvenile stand.

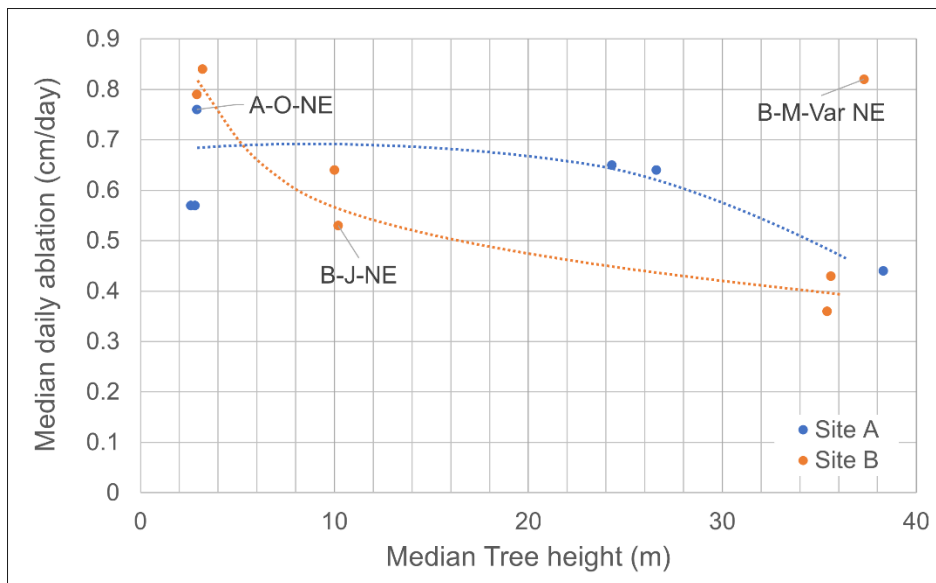


Figure 14. Trends in ablation rates with stand height.

There are no previous studies that have investigated ablation rates with tree height across aspects. Potter and others (2024) investigated stand-level ablation rates at a north-aspect, low elevation (1000m asl) site in Rover Creek that included 10- and 15-meter juvenile stands. They reported decreases in stand level ablation rates with increasing tree height for ablation rates measured over a 1-week period. A previous BC study of ablation rates in spruce and pine forests in low gradient terrain which included open, juvenile (4.5m), juvenile thinned (6.4m) and mature stands reported decreased ablation rates with increasing canopy density but also reported higher ablation rates in the thinned juvenile stands than in an adjacent clearcut for the first 2 weeks of the full melt period (Winkler et al, 2005). Although ablation rates were not explicitly studied, Ellis and others (2011) documented similar SWE volumes and depletion patterns for mature forested sites on north and south aspects which, as noted above, they attribute to similarities in total net longwave and shortwave energy through the melt period beneath the mature forest canopy.

### 3.4 Hydrological Recovery of Peak SWE and Ablation with Tree Height

Hydrological recovery of April 20<sup>th</sup> peak SWE and ablation rates for the juvenile stands in both Sites A and B are calculated using Equation 3.

#### PEAK SWE RECOVERY

Different patterns of Peak SWE recovery were observed for Sites A and B. The visually approximated recovery curve for Site A increases gradually between the open and advanced juvenile stands then increases more rapidly between the juvenile and mature stand (blue curve, Figure 15). The substantial difference in peak SWE recovery observed in the juvenile stands in Site B (orange curves, Figure 15) highlights the problem in defining a trend with only two intermediate data points. In Site B both juvenile stands include regenerating trees of similar height, crown cover and stem density (Table 7), however, the B-J-NE stand is over four times larger in area than the B-J-E stand. The greater spatial extent of the B-J-NE stand decreases the possibility of bias in the measured SWE associated with local factors such as a higher percentage of open patches, edge effects or local topographic effects. The orange dashed line in Figure 15 approximates the recovery of peak SWE in Site B stands given the likelihood that the B-J-NE is more representative of peak SWE response within a juvenile stand for this location. SWE recovery in stands B-J-E (which is set to -100) and B-M-Var-NE are negative because the April 20<sup>th</sup> peak SWE in these stands is higher than in the adjacent open stands.

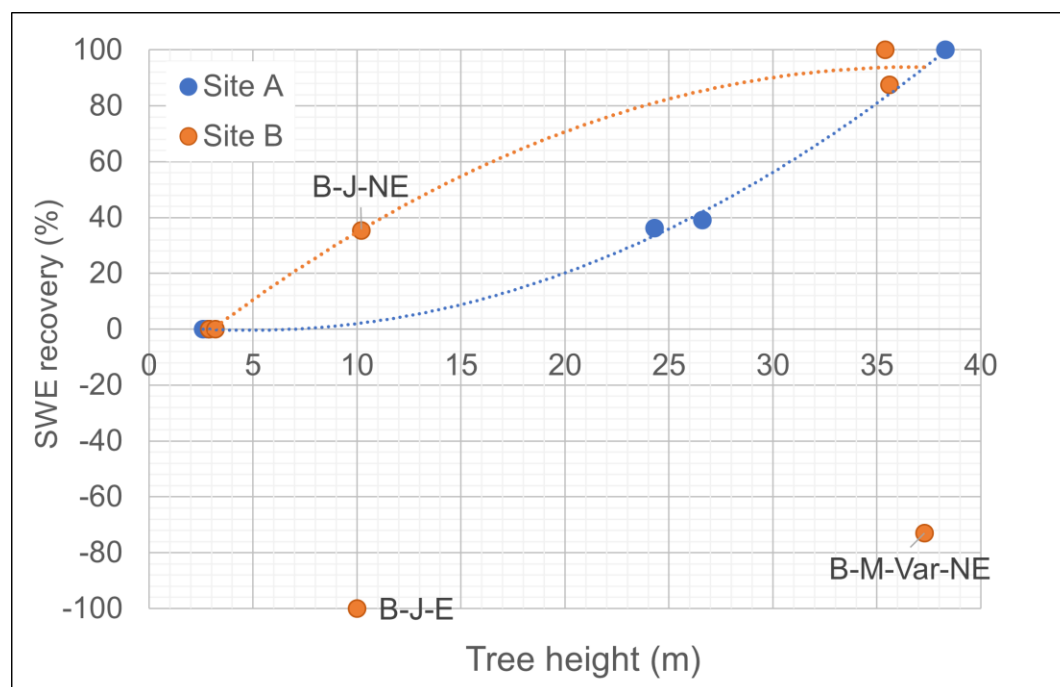


Figure 15. April 20<sup>th</sup> Peak SWE recovery for juvenile stands in Sites A and B. Orange dash-dot visually estimated curve assumes that stand B-J-E is influenced by unknown factors and represents an outlier in SWE behavior.

The faster recovery of peak SWE observed at Site B (considering only stand B-J-NE) is consistent with peak SWE recovery rates observed by Buttle and others (2005) in low-relief spruce dominated stands in

the boreal forests of northern Ontario and, as well, consistent with the rate of peak SWE recovery observed by Winkler and others (2005) also for low relief, spruce and pine stands in the Thompson – Okanagan highlands. The slower recovery of peak SWE observed for the advanced juvenile north and northeast stands of Site A has not previously been reported however, based on the process-understanding gained from studies in low-relief terrain and steeper terrain of the Rocky Mountains, it is consistent with the combined influence of smaller forest crown height, which would reduce the interception capacity of the juvenile forest relative to the mature forest, and lower total net energy at the snow surface through the early melt period in the north-aspect stands, which would preserve the beneath-canopy snowpack through the early melt period (Winkler, 2001; Ellis et al., 2011).

#### ABLATION RECOVERY

Ablation recovery was calculated (using Equation 3) for the juvenile stands in Site A relative to the average of the median ablation rates for the three open stands (A-O-NW, A-O-N and A-O-NE) and the average of the median ablation rates for the three mature stands (A-M-NW, B-M-E and B-M-NE). Ablation recovery was calculated for the juvenile and variable mature retention stands of Site B relative to the average of the median ablation rates for the two open stands of Site B (B-O-E and B-O-SE) and the average of the median ablation rates for the three mature stands.

Substantially different visual trends in ablation recovery were observed for Sites A and B (Figure 16). The Site A ablation recovery appears very slow due to slightly higher ablation rates in the advanced juvenile stands relative to the open stands. In contrast the recovery curve defined using juvenile stands of Site B indicates a relatively rapid recovery between the open stands and the 10m juvenile stands which both record lower ablation rates for the April 20<sup>th</sup> to May 19<sup>th</sup> period compared to the adjacent open stands. Of the two juvenile stands B-J-NE indicates a larger recovery in ablation rate than the adjacent B-J-E stand. In contrast ablation recovery in the Mature-Variable-NE stand of site B is lower than observed in the adjacent juvenile stands.

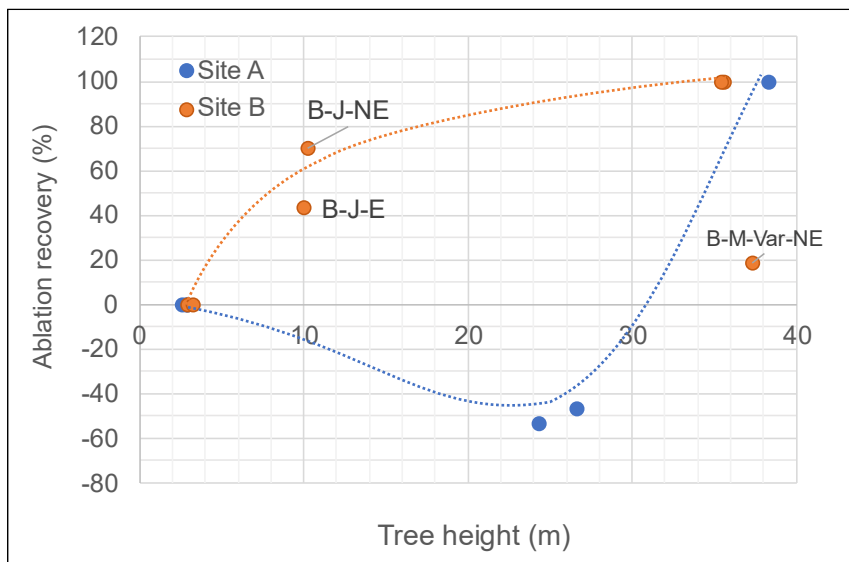


Figure 16. April 20<sup>th</sup> to May 19<sup>th</sup> ablation rate recovery by tree height for Site A and B. Recovery curves for Sites A (blue) and B (orange) are fitted visually.



Differences in ablation recovery trends at Site A and B relate to the differences in ablation rates between the open and juvenile stands in both sites. The two juvenile stands of Site A recorded similar April 20<sup>th</sup> to May 19<sup>th</sup> ablation rates (Table 9Rya) which were slightly higher than the mean ablation rate for the three open stands resulting in negative recovery in ablation rates with regenerating stands up to 25m height and then a rapid recovery in ablation rates beyond this point. In contrast the juvenile stands in Site B both displayed decreased ablation rates relative to the open stands so that the ablation recovery proceeds quickly from the 3m open stand to the 10m juvenile stands and then gradually from the 10m stand height to the fully mature stands.

The finding of substantially delayed ablation recovery in advanced juvenile north and northeast stands of Site A has not been reported previously. Potter and others (2024) observed increasing ablation recovery with increasing tree height in northeast juvenile and advanced juvenile stands relative at lower elevations in Rover Creek, but they also found increasing variability in ablation recovery in juvenile stands with increasing tree height. Based on the findings of Ellis and others (2011) from their study of aspect effects on snow accumulation and melt in the Rocky Mountains, the delay in ablation recovery in the juvenile north aspect stands is likely attributable to a delay in the recovery of the below-crown total net longwave energy balance. Ellis and others (2011) and Ellis and others (2013) found that in north aspect mature stands snowmelt is dominated by longwave radiation which increases with increasing canopy density. The Ellis studies also reveal the much higher total net energy measured in south aspect clearcuts compared to north aspect clearcuts. They were able to relate the delayed snow disappearance in the north aspect clearcuts compared to the adjacent north aspect forested stands to lower net longwave radiation from the absence of the forest canopy.

## 4.0 Discussion

This study demonstrates the value of high-resolution UAV LiDAR-derived snow surface models for investigating the influence of forest stand maturity and slope aspect on snow accumulation (peak SWE) and ablation dynamics in mountainous terrain. By capturing spatially continuous snow depth data throughout the melt season, we were able to characterize stand-level snow processes with unprecedented detail and assess stand maturity effects and hydrological recovery across a range of forest conditions.

### Forest Maturity and Peak SWE

Our results confirm that forest maturity significantly influences peak SWE, with open stands consistently exhibiting higher peak SWE than juvenile and mature stands. This trend aligns with previous findings (e.g., Winkler et al., 2005; Ellis et al., 2011), which attribute reduced peak SWE in forested areas to increased interception and shading. However, the magnitude of SWE reduction varied by aspect and stand structure. Notably, the advanced juvenile stands in Site A (north and northeast aspects) recorded peak SWE values closer to Site A open stands, suggesting that canopy structure, including tree height and crown cover play a different role in snow retention in the absence of higher net shortwave radiation.

Interestingly, the variable retention mature stand (B-M-Var-NE) exhibited SWE values only slightly higher than fully forested mature stands, indicating that retained canopy (~60% cover) continues to exert an influence on snow accumulation. This finding supports the hypothesis that partial canopy retention can contribute to snow interception capacity, though the energy balance implications remain uncertain.

## Forest maturity and Ablation

Our findings confirm an inverse relationship between ablation rate and forest maturity, however, as with peak SWE, this relationship is strongly influenced by both canopy structure and stand aspect. Ablation rates in Site A open stands are higher than recorded in the adjacent mature stands while the advanced juvenile stands of Site A displayed ablation rates nearer to that of the open stands. This was not the case in Site B where open stands (southeast and east) displayed substantially higher ablation rates than observed in the juvenile (northeast and east) stands which were, in turn, higher than the mature (northeast and east) stands. The ablation rates observed in all three mature stands were similar regardless of aspect supporting the critical moderating effect of the mature forest stand on the snow surface net energy balance. These observations are consistent with the findings of Ellis and others (2011 and 2013) who showed that the ablation rates of open stands on contrasting north and south aspects are substantially different in response to differences in net shortwave radiation while the adjacent mature stands with contrasting aspects display similar snowmelt rates.

## Aspect Effects on peak SWE and Ablation

Aspect emerged as a dominant control on peak SWE variability in open stands, with Site A's north and northwest aspects accumulating significantly more snow than Site B's east and southeast aspects. This pattern is consistent with studies in the Rocky Mountains (Ellis et al., 2011), where higher net shortwave radiation on south-facing slopes accelerates snowmelt through the accumulation period and reduces net accumulation. In contrast, mature stands showed minimal SWE differences across aspects, suggesting that dense canopy cover buffers the snowpack from aspect-driven energy inputs.

Ablation rates followed similar patterns, with open stands on east and southeast aspects (Site B) exhibiting the highest melt rates. Mature stands, regardless of aspect, had the lowest ablation rates, reinforcing the role of canopy shading in moderating snowmelt. Juvenile stands displayed intermediate behavior, with Site B's juvenile stands showing more rapid ablation recovery than those in Site A, likely due to differences in canopy structure and local microclimate.

## Hydrological Recovery Patterns

Hydrological recovery, expressed as a percentage of mature stand versus open stand conditions, varied markedly between sites. In Site A (north aspects), peak SWE recovery progressed slowly with increasing stand height, while ablation recovery was delayed or even negative in juvenile stands. This suggests that while snow accumulation may begin to recover with canopy development, the energy balance beneath juvenile canopies may still promote rapid melt due to insufficient longwave radiation input.

In contrast, Site B (east aspects) showed more rapid recovery in both peak SWE and ablation rates, particularly in the juvenile NE stand. However, inconsistencies between adjacent juvenile stands (e.g., B-J-E vs. B-J-NE) highlight the influence of local topography, stand size, and potential edge effects. These findings underscore the complexity of hydrological recovery in mountainous terrain and caution against applying generalized recovery curves without site-specific calibration.

## Unexpected Results and Outliers

Several stands deviated from expected trends. For example, A-O-NE exhibited lower peak SWE than adjacent open stands which is likely attributed to microclimate differences. A-O-NE possibly receives additional longwave energy from the opposite southwest aspect valley slope which would also account for the slightly increased ablation rate observed in the NE open stand relative to the two adjacent open stands (N and NW). Lower peak SWE and lower ablation rates in B-J-NE compared to adjacent B-J-E may also be due to microtopographic differences between the two stands, however, in this case the relatively small size of B-J-E and proximity of this stand to the mature stand may be influencing snow processes. Lastly, the low peak SWE but high ablation rate in B-M-Var-NE suggests that the more open canopy structure may increase energy availability at the snow surface, despite the retained crown cover.

## Implications and Future Directions

This study advances our understanding of snow-forest interactions by integrating UAV LiDAR with detailed stand metrics and aspect analysis. The findings have direct implications for forest management and hydrological modeling, particularly in the context of post-disturbance recovery and climate change adaptation. However, the results also highlight the need for:

- Additional LiDAR based investigations in stands where canopy structure and microtopography can be better controlled.
- Direct snow density measurements to improve stand-level SWE estimates.
- Additional measurements of net radiation beneath forest stands to improve modeling of energy balance beneath partial canopies and across complex terrain.

Future work should integrate process-based forest growth and snow models (e.g., Raven, Craig et al., 2020) with LiDAR-derived metrics to simulate hydrological recovery under different management and climate scenarios.

## 5.0 Conclusions

This study demonstrates the effectiveness of UAV LiDAR in capturing high-resolution snow surface data to assess the influence of forest stand maturity and slope aspect on snow accumulation and ablation dynamics in mountainous terrain. By analyzing snow depth and SWE across a range of forest conditions and aspects, we were able to quantify hydrological recovery patterns with unprecedented spatial detail.

## Key findings include:

Forest maturity significantly influences snow processes: Open stands consistently exhibited higher peak SWE and faster ablation rates than juvenile and mature stands. Mature stands, regardless of aspect, showed the lowest ablation rates, highlighting the role of canopy shading in moderating snowmelt.

Aspect is a dominant control in open stands: Northeast through northwest-facing open stands (Site A) accumulated more snow and melted more slowly than east and southeast-facing open stands (Site B), consistent with known energy balance dynamics.

Hydrological recovery varies by site and metric: Recovery of peak SWE and ablation rates with increasing stand height followed different trajectories in Sites A and B. Site A (north aspects) showed slower recovery, particularly for ablation, while Site B (east aspects) exhibited more rapid recovery, though with notable variability between adjacent juvenile stands.

Partial canopy retention influences snow dynamics: The variable retention mature stand (B-M-Var-NE) behaved more like an open stand in terms of ablation, suggesting that altered canopy structure can increase energy availability at the snow surface despite retained crown cover.

Outliers highlight the complexity of mountainous terrain: Stands such as A-O-NE and B-J-E deviated from expected trends, emphasizing the importance of local topography, elevation range, and microclimatic effects in shaping snowpack behavior.

Overall, this research advances our understanding of snow-forest interactions and provides a foundation for improving hydrological models and forest management strategies in snow-dominated mountain watersheds. The integration of UAV LiDAR with stand-level metrics offers a powerful tool for assessing post-disturbance recovery and informing climate adaptation planning.

## 6.0 Citations

B.C. Ministry of Environment, (1981). Snow Survey Sampling Guide. Downloaded from [www2.gov.bc.ca/assets/gov/environment/air-land-water/water/snow/snow\\_survey\\_sampling\\_guide.pdf](http://www2.gov.bc.ca/assets/gov/environment/air-land-water/water/snow/snow_survey_sampling_guide.pdf)

Buttle, J. M., Oswald, C. J., and Woods, D. T. (2005). Hydrologic Recovery of Snow Accumulation and Melt Following Harvesting in Northeastern Ontario. 62nd Eastern Snow Conference. Waterloo, ON, Canada.

CloudCompare version unknown (2022). CloudCompare - 3D point cloud and mesh processing software. Retrieved from <https://www.cloudcompare.org/>

Deems, J. S., & Painter, T. H. (2006). Lidar measurement of snow depth: accuracy and error sources. *Proceedings of the 2006 International Snow Science Workshop: Telluride, Colorado, USA, International Snow Science Workshop*, 330, 330–338.

Deems, J. S., Painter, T. H., & Finnegan, D. C. (2013). Lidar measurement of snow depth: A review Lidar measurement of snow depth: a review. *Journal of Glaciology*, 59, 467–479.

<https://doi.org/10.3189/2013JoG12J154>

Deenik, K., Busseau, B., Green, K., & Potter C., (2022). Deriving Snow Surface Elevations from LiDAR: A Comparison Between Aerial and Ground-based Methods in Mountainous Forest Stands. Poster C42F-1090 presented at AGU 2022. <https://ui.adsabs.harvard.edu/abs/2022AGUFM.C42F1090D/abstract>

Ellis, C. R., Pomeroy, J. W., Essery, R. L. H., & Link, T. E. (2011). Effects of needleleaf forest cover on radiation and snowmelt dynamics in the Canadian Rocky Mountains. *Can. J. For. Res.*, 41, 608–620.

<https://doi.org/10.1139/X10-227>

Ellis, C. R., Pomeroy, J. W., & Link, T. E. (2013). Modeling increases in snowmelt yield and desynchronization resulting from forest gap-thinning treatments in a northern mountain headwater basin, 49, 936–949. <https://doi.org/10.1002/wrcr.20089>

Jost, G., Weiler, M., Gluns, D.R., & Alila, Y., (2007). The influence of forest and topography on snow accumulation and melt at the watershed-scale. *J. Hydrol.* 347, 101-115.

Khalilzadeh, J., & Tasci, A. D. (2017). Large Sample Size, Significance Level, and the Effect Size: Solutions to Perils of Using Big Data for Academic Research. *Tourism Management*, 62, 89-96.

<https://doi.org/10.1016/j.tourman.2017.03.026>

Potter, C., 2024. Forest stand hydrological recovery of snow accumulation and ablation investigated using simultaneous localization and mapping (SLAM) enabled LiDAR. MSc Thesis, University of Victoria, BC., Canada., 97p. <https://hdl.handle.net/1828/20834>.

Potter, C., Green, K.C., Peters, D., & Niemann, K. (2024). Investigating hydrological recovery in regenerating coniferous stands in snow-dominated watersheds using simultaneous localization and mapping-enabled mobile terrestrial LiDAR. *Hydrological Processes*, 38(7), e15247.

<https://doi.org/10.1002/hyp.15247>

Hudson, R. (2000). Snowpack recovery in regenerating coastal British Columbia clearcuts. *Canadian Journal of Forest Research*, 30(4), 548.

Isenburg, M. (2022\*\*). LASTools – Efficient LiDAR Processing Software. Retrieved from

<https://rapidlasso.com/lastools>

PDAL Contributors. (2022\*\*). PDAL - Point Data Abstraction Library [Computer software]. Retrieved from <https://pdal.io>

Roussel, J.-R., & Auty, D. (2022\*\*). lidR: Airborne LiDAR Data Manipulation and Visualization for Forestry Applications. Available at: <https://cran.r-project.org/package=lidR>

Varhola, A., Coops, N. C., Weiler, M., & Moore, R. D. (2010). Forest canopy effects on snow accumulation and ablation: An integrative review of empirical results. *Journal of Hydrology*, 392(3–4), 219–233.

<https://doi.org/10.1016/j.jhydrol.2010.08.009>



Winkler, R.D. (2001). The effects of forest structure on snow accumulation and melt in south-central British Columbia, PhD thesis. University of British Columbia, Vancouver, B.C.  
<https://open.library.ubc.ca/soa/cIRcle/collections/ubctheses/831/items/1.0090837?o=10>

Winkler, R. D., & Moore, R. D. (2006). Variability in snow accumulation patterns within forest stands on the interior plateau of British Columbia, 3695, 3683–3695. <https://doi.org/10.1002/hyp>

Winkler, R.D., Spittlehouse, D.L. & Golding, D.L. (1995), The Importance of Sample Size in Forest/Clearcut Snow Accumulation Comparisons. Mountain hydrology, Peaks and Valleys in Research and Applications. Proceedings from a conference, May 16-19, 1995, Vancouver, British Columbia.






Winkler, R.D., Spittlehouse, D.L. & Golding, D.L. (2005), Measured differences in snow accumulation and melt among clearcut, juvenile, and mature forests in southern British Columbia. *Hydrol. Process.*, 19: 51-62. <https://doi.org/10.1002/hyp.5757>

Winkler, R., Moore, D., Redding, T, Spittlehouse, D. & Smerdon, B. (2010). The Effects of Forest Disturbance on Hydrologic Processes and Watershed Response, Chapter 7. In: Pike, R.G., T.E. Redding, R.D. Moore, R.D. Winkler, and K.D. Bladon (editors). 2010.

Winkler R.D. & Boon, S., (2015), Revised Snow Recovery Estimates for Pine-Dominated Forests in Interior British Columbia. B.C. Ministry of Forests, Lands and Natural Resource Operations, Extension Note 116 (<https://www.for.gov.bc.ca/hfd/pubs/docs/en/EN116.PDF>).

## Appendix 1. Equipment used in field data collection

RPAS and sensors used for data acquisition.

Model and Manufacturer	Purpose	Specs	Photo + Product Link
<b>RPAS</b>			
DJI Matrice 300 RTK	2.7 kg load capable medium size enterprise UAV that allows swappable (and multiple) sensor integration	15km max transmission 55 min max flight time 7000m service ceiling 12m/s max wind speed resistance 23m/s max speed -20 to 50°C operating temp IP45 rating 6-directional sensing and positioning Hot-swappable battery Anti-Collision Beacon	 <a href="https://enterprise.dji.com/matrice-300">https://enterprise.dji.com/matrice-300</a>
<b>Sensors</b>			
DJI Zenmuse L1 LiDAR + RGB	For collection of LiDAR and RGB imagery	<u>Livox LiDAR:</u> Wavelength = 905nm Accuracy H = 10cm V = 5cm Point Rate = 240,000 pts/s FOV H = 360, V = 100 Working range = 0.1-100m Returns = 3 Detection Range = 450m (80% reflectivity, 0 klx) / 190 m (10% reflectivity, 100 klx)	 <a href="https://enterprise.dji.com/zenmuse-l1">https://enterprise.dji.com/zenmuse-l1</a>
		<u>RGB Camera:</u> 1" CMOS on a 3-axis stabilized gimbal 20MP, mechanical shutter High accuracy IMU	
Geoslam Zeb Horizon scanner	For collection of LiDAR data	300,000 scanner points per second Accuracy = 6mm Range = 100m FOV = 360° x 270°	 <a href="https://geoslam.com/solutions/zeb-horizon/">https://geoslam.com/solutions/zeb-horizon/</a>
<b>GNSS</b>			
Stonex S900 Basestation	For GPS corrections and improved precision	2 cm accuracy 30° 5 cm accuracy 60°	 <a href="https://www.stonex.it/project/s900-plus-gnss-receiver/">https://www.stonex.it/project/s900-plus-gnss-receiver/</a>
Trimble GPS	For collection of points, lines and polygon features	10 mm H/20 mm V RTK Precision	 <a href="https://geospatial.trimble.com/en/products/hardware/trimble-r2">https://geospatial.trimble.com/en/products/hardware/trimble-r2</a>

## Appendix 2 - Snow Water Equivalent from Snow Depth – Investigation of snow density derivation approaches

Given the limited number of snow core samples collected (approximately eight per site during the 2020 winter season), we adopted a variety of methods to enhance our understanding of snowpack dynamics and, specifically, snow density trends over time within the study area. The approaches ranged from simple interpolation techniques to complex statistical models to address the intricacies of snow density, snow water equivalent (SWE), and snow depth.

Initially simple interpolation methods were investigated:

**Na.Approx:** Employs a linear interpolation of missing values, suitable for simpler datasets where changes between points are expected to be linear.

To more accurately reflect the complex and nonlinear behaviors observed in the snowpack data, we incorporated several advanced modeling techniques:

**Polynomial and Linear Regression:** Polynomial regression addresses the non-linear relationships and varying rates of change in snow density as depth increases, which are crucial for detailed hydrological modeling. Concurrently, linear regression's simplicity provides a baseline for understanding general trends, such as the typical increase of SWE with snow depth.

These techniques were integrated to conduct a thorough analysis of the sparse snow core data.

Advanced models like LOESS and GAM allowed for nuanced exploration of localized data characteristics, while polynomial and linear regressions helped establish foundational relationships and trends. The Fourier series complemented these by capturing periodic fluctuations, enriching our overall model's predictive power and reliability.

This integration of multiple modeling approaches not only addressed the challenge of data scarcity but also enhanced the depth and reliability of our understanding of snow depth to SWE relationships, facilitating robust predictions that can adapt to varying winter conditions.

### MODEL SELECTION

More complex models such as polynomial regression (2nd and 3rd degree) and non-parametric LOESS regression showed varying performance. The LOESS models generally performed well, with  $R^2$  values consistently above 0.96, indicating a good fit, while the 3rd-degree polynomial models achieved moderate success, with  $R^2$  values around 0.76 to 0.81. The 2nd-degree polynomial models underperformed, with  $R^2$  values ranging from 0.33 to 0.45, suggesting a simpler model structure failed to capture SWE dynamics as a function of day of the year effectively (Table 10).

At the conclusion of this analysis, we determined that using day of the year as a predictor introduced assumptions that did not fully account for variability between winter seasons, which could drastically affect SWE dynamics and reduce the model's effectiveness between years. As a result, we shifted to an alternative approach based on SWE as a function of snow depth, aiming to better capture snowpack behaviour without the limitations imposed by calendar-based models. In the following section, we explore how a linear regression model, using snowpack depth as a predictor of SWE, provides a more intuitive and flexible approach to understanding SWE variability.

Table 10. Snow density approximation models  $R^2$  performance

Stand	Na.Approx	Na.spline	Linear	Polynomial 2 <sup>nd</sup> degree	Polynomial 3 <sup>rd</sup> degree	Loess	GAM	Fourier
Site A-M	1	1	1	0.43	0.82	0.98	0.98	0.70
Site A-O	1	1	1	0.45	0.76	0.98	0.97	0.67
Site B-J	1	1	1	0.38	0.81	0.97	0.97	0.63
Site B-M	1	1	1	0.33	0.79	0.98	0.97	0.68
Site B-O	1	1	1	0.44	0.79	0.96	0.96	0.60

#### Linear SWE to Depth Functions

The linear approach offered a clear advantage in that it assumes a direct positive relationship between snow depth and SWE, simplifying the process of estimation and interpretation. In this case, the high  $R^2$  values observed across the sites confirmed the adequacy of the model in capturing the underlying relationship between snow depth and SWE, making it an effective tool. SAU-O achieved the highest  $R^2$  value (0.999), while the lowest value was with the NAU-O site (0.966). As a result, we decided to use this method to improve the clarity of the depth to SWE relationships for implementation on the snow depth raster files (outlined in the next section), while also maintaining flexibility and avoiding the limitations that came with more complex approaches or calendar-based assumptions (Figure 21).

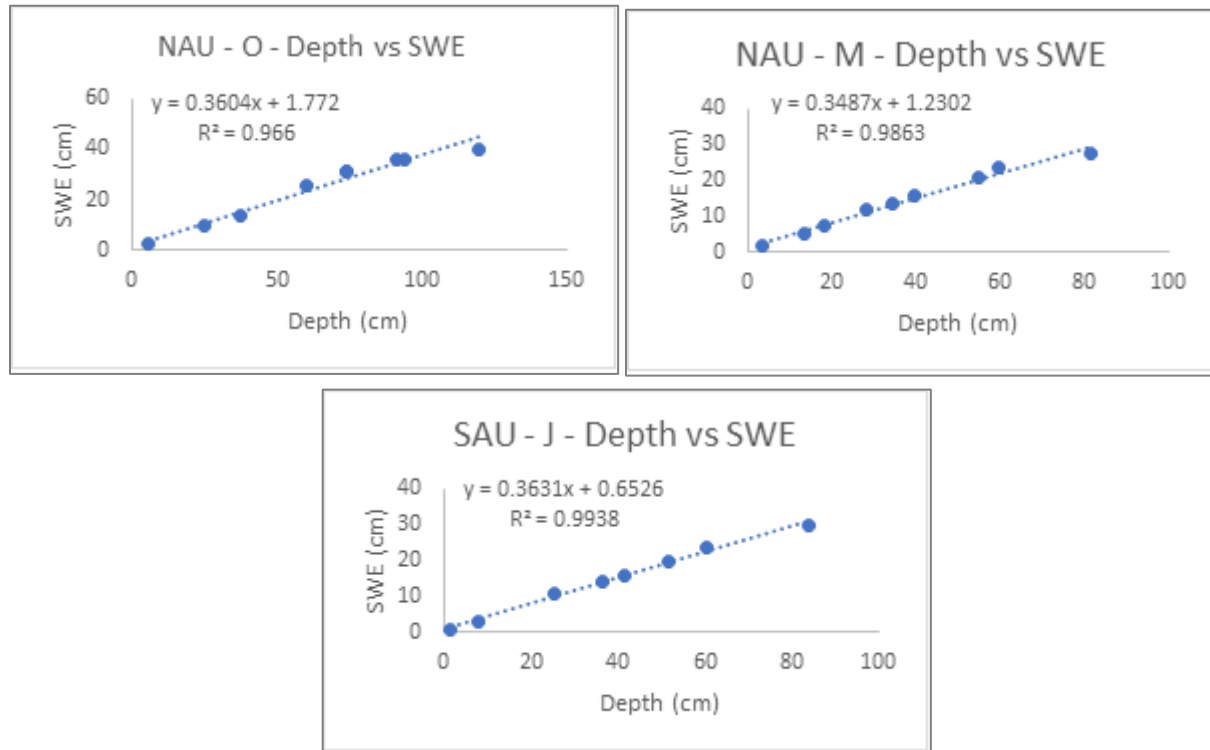


Figure 17. SWE to depth relationships developed for a range of stands using adjusted 2020 field measurements.

## Appendix 3. Statistical test results

HISTOGRAMS OF RASTER VALUES FOR PEAK SWE AND ABLATION FOR ALL STANDS ARE SHOWN IN FIGURES 17 AND 18.

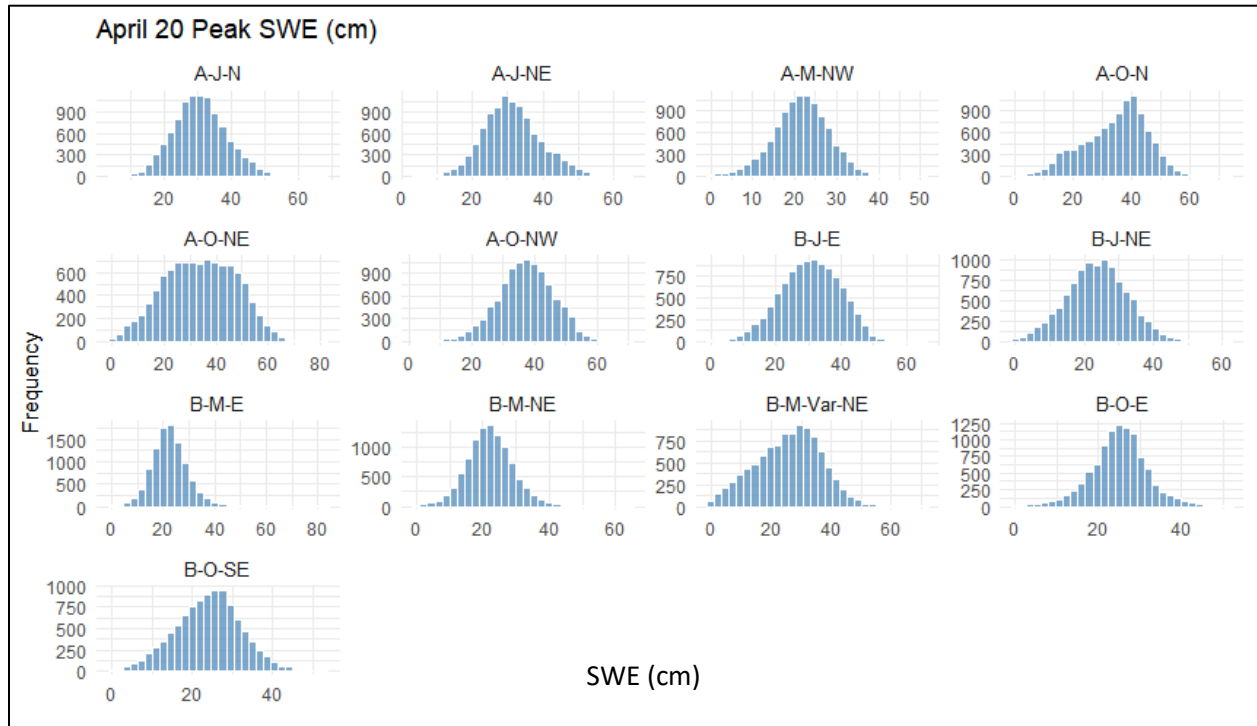


Figure 18. Histograms for peak SWE rasters for all sites.

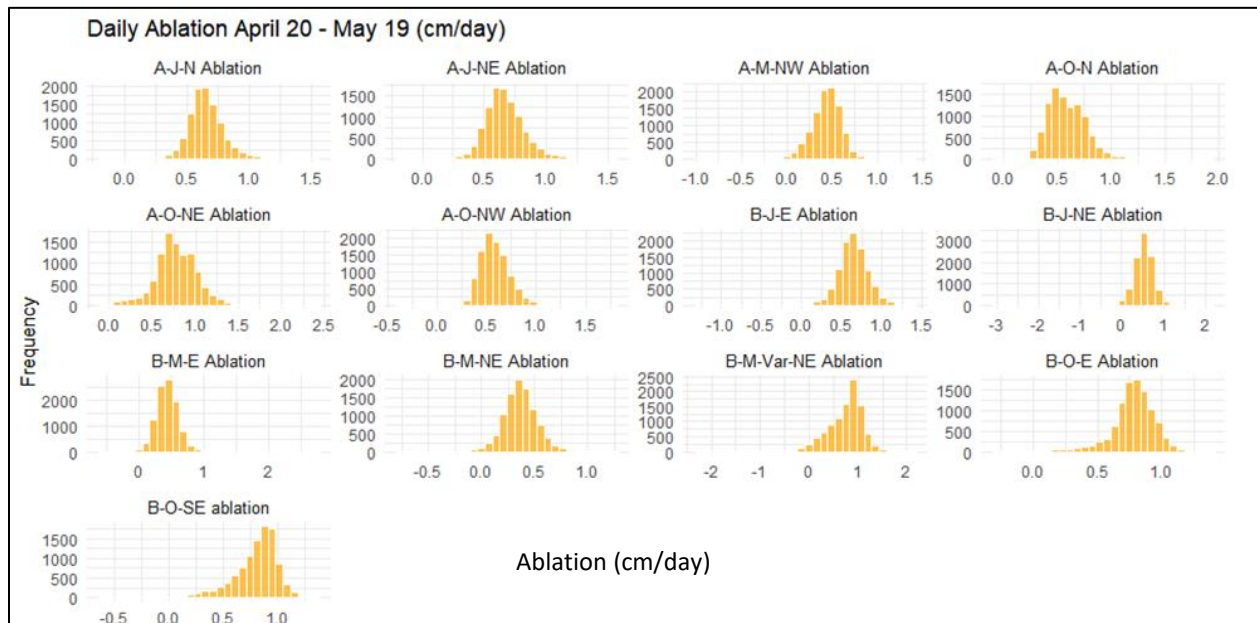


Figure 19. Histograms for ablation rasters for all sites.



## Q-Q PLOTS TO INVESTIGATE NORMALITY FOR PEAK SWE AND ABLATION RASTERS.

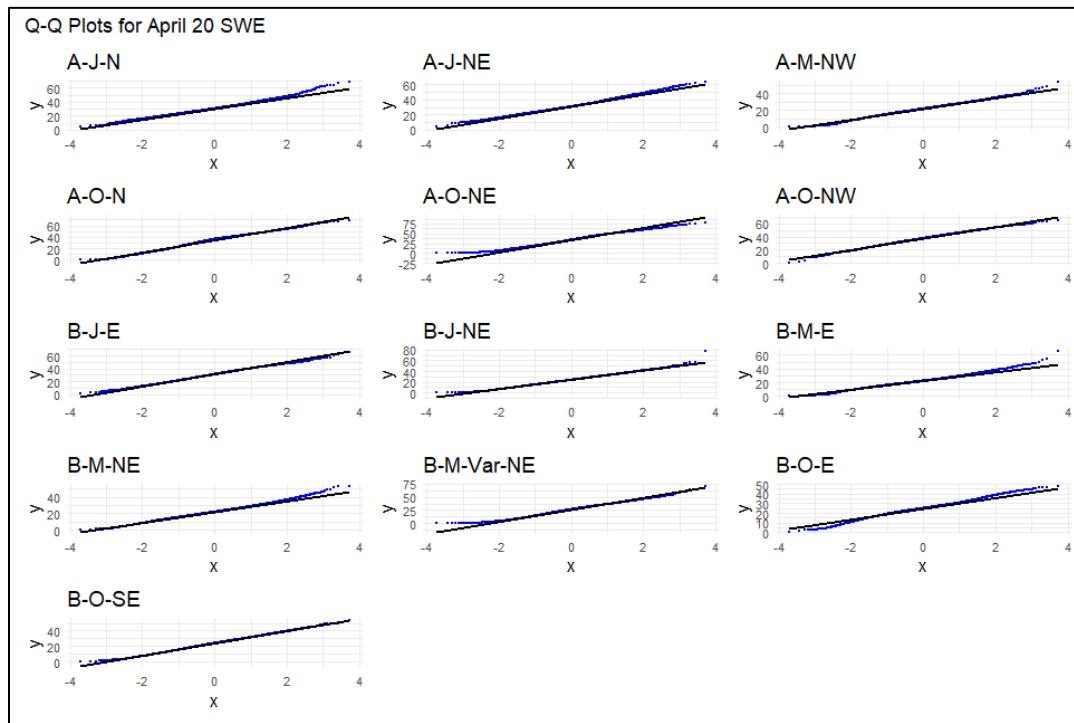


Figure 20. Q-Q plots for peak SWE rasters for all sites.

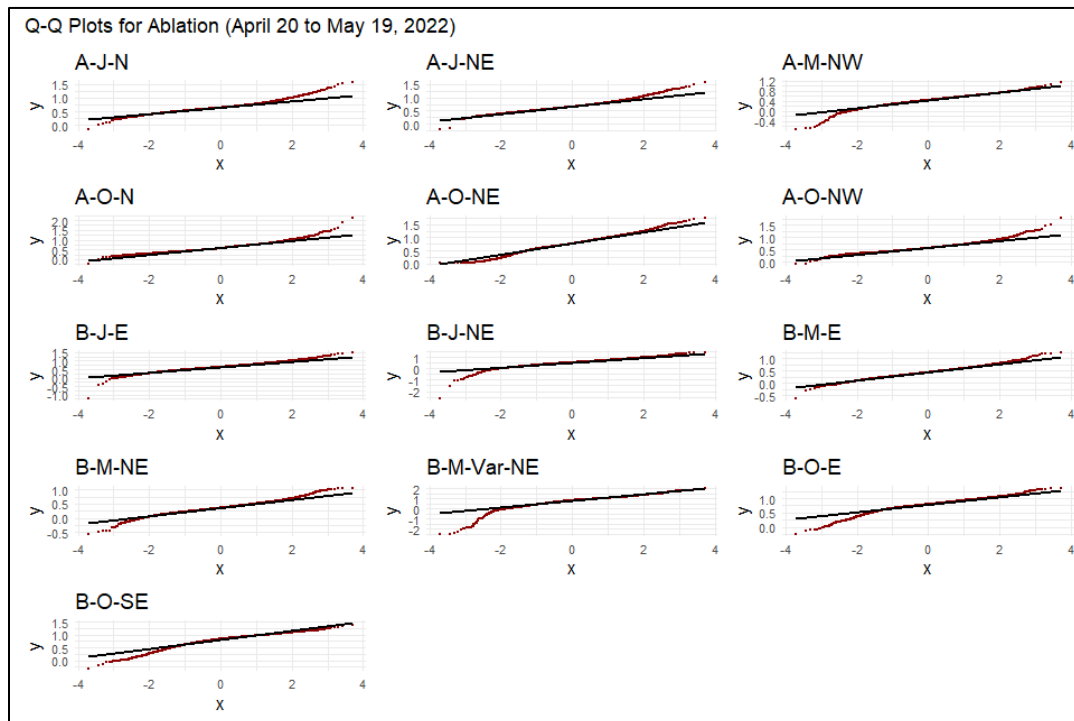


Figure 21. Q-Q plots for ablation rasters for all sites.

**COHEN'S D ANALYSIS TO DETERMINE STATISTICAL SIGNIFICANCE OF SIMILARITIES FOR PEAK SWE AND ABLATION FOR ALL STANDS IN SITES A AND B**

*Table 11. Effect size (Cohen's d) for comparing mean peak SWE between stands.*

TREATMENT	CONTROL													
		A-O-NW	A-O-N	A-O-NE	A-J-N	A-J-NE	A-M-NW	B-O-E	B-O-SE	B-J-E	B-J-NE	B-M-E	B-M-NE	B-M-Var-NE
	A-O-NW	0.00	0.25	0.25	0.81	0.73	2.38	1.85	1.65	0.73	1.55	2.13	2.16	1.07
	A-O-N	0.31	0.00	0.05	0.48	0.40	1.97	1.44	1.32	0.43	1.24	1.74	1.77	0.81
	A-O-NE	0.39	0.06	0.00	0.39	0.31	1.86	1.33	1.23	0.35	1.16	1.64	1.67	0.75
	A-J-N	0.75	0.35	0.23	0.00	0.07	1.39	0.86	0.85	0.01	0.80	1.19	1.23	0.46
	A-J-NE	0.68	0.29	0.18	0.08	0.00	1.48	0.95	0.93	0.08	0.87	1.28	1.31	0.51
	A-M-NW	1.80	1.19	0.90	1.15	1.21	0.00	0.53	0.28	1.00	0.25	0.14	0.09	0.40
	B-O-E	1.40	0.87	0.64	0.71	0.78	0.53	0.00	0.15	0.62	0.15	0.36	0.41	0.07
	B-O-SE	1.54	0.98	0.73	0.86	0.93	0.35	0.18	0.00	0.75	0.01	0.19	0.24	0.19
	B-J-E	0.76	0.36	0.23	0.01	0.09	1.38	0.85	0.84	0.00	0.79	1.17	1.21	0.45
	B-J-NE	1.55	0.99	0.74	0.88	0.94	0.33	0.20	0.01	0.76	0.00	0.17	0.23	0.20
	B-M-E	1.69	1.10	0.82	1.03	1.09	0.15	0.38	0.16	0.89	0.14	0.00	0.06	0.31
	B-M-NE	1.74	1.14	0.85	1.08	1.14	0.09	0.44	0.21	0.93	0.18	0.06	0.00	0.35
	B-M-Var-NE	1.31	0.80	0.58	0.61	0.68	0.65	0.12	0.25	0.53	0.24	0.48	0.53	0.00

*Table 12. Effect size (Cohen's d) for comparing mean ablation rate between stands*

TREATMENT	CONTROL													
		A-O-NW	A-O-N	A-O-NE	A-J-N	A-J-NE	A-M-NW	B-O-E	B-O-SE	B-J-E	B-J-NE	B-M-E	B-M-NE	B-M-Var-NE
	A-O-NW	0.00	0.00	0.75	0.43	0.44	0.94	1.19	1.05	0.28	0.28	0.88	1.38	0.39
	A-O-N	0.00	0.00	0.75	0.43	0.44	0.94	1.19	1.05	0.28	0.28	0.88	1.38	0.39
	A-O-NE	1.20	1.00	0.00	0.86	0.69	2.00	0.06	0.15	0.72	1.00	1.94	2.50	0.08
	A-J-N	0.40	0.33	0.50	0.00	0.06	1.29	0.81	0.75	0.06	0.52	1.24	1.75	0.24
	A-J-NE	0.47	0.39	0.46	0.07	0.00	1.35	0.75	0.70	0.11	0.56	1.29	1.81	0.21
	A-M-NW	1.07	0.89	1.42	1.57	1.44	0.00	2.19	1.85	1.17	0.36	0.06	0.38	0.82
	B-O-E	1.27	1.06	0.04	0.93	0.75	2.06	0.00	0.10	0.78	1.04	2.00	2.56	0.11
	B-O-SE	1.40	1.17	0.13	1.07	0.88	2.18	0.13	0.00	0.89	1.12	2.12	2.69	0.16
	B-J-E	0.33	0.28	0.54	0.07	0.13	1.24	0.88	0.80	0.00	0.48	1.18	1.69	0.26
	B-J-NE	0.47	0.39	1.04	0.93	0.88	0.53	1.63	1.40	0.67	0.00	0.47	0.94	0.58
	B-M-E	1.00	0.83	1.38	1.50	1.38	0.06	2.13	1.80	1.11	0.32	0.00	0.44	0.79
	B-M-NE	1.47	1.22	1.67	2.00	1.81	0.35	2.56	2.15	1.50	0.60	0.41	0.00	0.97
	B-M-Var-NE	1.00	0.83	0.13	0.64	0.50	1.82	0.25	0.30	0.56	0.88	1.76	2.31	0.00

301 Frank Beinder Way,  
Castlegar, BC V1N 4L3  
*phone* **250.365.7292**  
*toll free* **1.888.953.1133**  
*email* **info@selkirk.ca**